BUDAPEST UNIVERSITY
OF TECHNOLOGY AND ECONOMICS

Master's Thesis

On the Convergence of Fourier Coefficients in Iterative SPECT Reconstruction

Attila Andai

Thesis Supervisor: Dr. Dávid Légrády PhD
Associate Professor
Budapest University of Technology and Economics
Faculty of Natural Sciences
Institute of Nuclear Techniques
Department of Nuclear Techniques

BME

2026

MŰEGYETEM 1782

Szakdolgozat-választás

A hallgató neve:	specializációja:
A záróvizsgát szervező tanszék neve: Nukleáris Technika	

A témavezető neve: Dr. Légrády Dávid
- tanszéke: Nukleáris Technika
- beosztása: egy. docens
- email címe: legrady@reak.bme.hu

A kidolgozandó feladat címe: Regularizáció a SPECT statisztikus iteratív képalkotásban

A téma rövid leírása, a megoldandó legfontosabb feladatok felsorolása:

Single Photon Emission Computed Tomography (SPECT) enjoys an importance burst due to the advance of theranosctics, a combination of cancer isotope therapy and diagnostics. Nuclear isotopes bound to tumour specific compounds find their ways to the proper place of irradiation by metabolism. Emitted short range radiation of charged particles (beta's and alpha's mostly) ensure a precise dose delivery to the cancer tissue while minimizing impact on organs at risk. Monitoring the delivery of radioisotopes is possible by the by-product gamma radiation. As the radiation mixture is optimized for dose delivery rather than for imaging, the SPECT measured data is suboptimal in many respect: either a low gamma yield or unfavourable gamma energy yield necessitate a leap forward in the quality of image reconstruction. Low intensity imaging and precise scatter signal removal requires the tailoring of reconstruction techniques towards ultimate precision.

Iterative statistical reconstruction schemes (Maximum Likelihood Expectation Maximization -MLEM, Primal-Dual Hybrid Gradient, etc) employs regularization to stabilise convergence and to direct the iteration towards favourable fixed points. The regularization is usually formulated as a constraint on e.g. the noise term: we prefer lower noise content of a reconstructed volume, or we would like to hinder the forming of image artefacts. A popular technique is the Total Variation (TV) norm (local sum of the absolute value of pixel intensity differences), that is often used in practice while its mathematical properties necessitate cumbersome approximations resulting in One Step Late (OSL) algorithms, or artefacts. TV norm with OSL-MLEM is notorious for creating chequerboard artefacts. Another example is the formation of the Gibbs-like artefact, where a certain spatial frequency above the resolution cut-off, become over-pronounced and adds a ringing to abrupt changes.

The task of the student is to create from existing building blocks a 2D ML-EM reconstruction sandbox in python, where the above mentioned TV regularization and the forming of the Gibbs artefact can be studied with different noise terms present. The properties of the regularization and Gibbs artefacts should be characterized. Some theoretically founded and some experimentally conjured algorithms are present in the scientific literature, such as forward projection biasing, sampling volume sharpening and inter-iteration filtering. The student shall experiment with these techniques, extend to inhomogeneous resolution problems and formulate solutions with sound theoretical bases and palpable image quality enhancements.

A záróvizsga kijelölt tételei:

Dátum: 2025. 02. 11.

Hallgató aláírása:	Témavezető aláírása*:	Tanszéki konzulens aláírása:	A témakiírását jóváhagyom (tanszékvezető aláírása):

Declarations

Declaration of originality

Undersigned Attila Andai, medical physics MSc student of the Budapest University of Technology and Economics, declare that I wrote this thesis without the use of any unauthorized assistance, under the guidance of my supervisor. I have cited every source I used. For any part that I have borrowed verbatim, or paraphrased while preserving its original meaning, I have marked its source of origin.

April 3, 2026

Identicality of digital and printed versions

Undersigned Attila Andai, medical physics MSc student of the Budapest University of Technology and Economics, declare that the digital and printed copies of the thesis are identical in all respects.

April 3, 2026

For now we see in a mirror, dimly, but then face to face.
Now I know in part; then I shall understand fully, even as I have been fully understood.

1 Corinthians 13:12

Contents

List of Figures

List of Videos

If this dissertation is being read in printed form, or if your PDF viewer does not support the playback of embedded videos, the videos can be accessed online via the QR codes provided below.

Figure 9: The reconstruction series of the cylindrical phantom.

Figure 12: The good Fourier components of the Fourier matrices through iterations.

Figure 16: The good Fourier vectors (with threshold minnorm = 0.1 and err = 0.25) through iterations for the sectoral phantom.

Figure 19: The good Fourier components of the Fourier matrices through iterations for the sectoral phantom.

Figure 27: Activity values of the 100th iteration of the above mentioned phantom at different radii.

Acknowledgements

I would like to express my deepest gratitude to my supervisor, Dávid Légrády, for many discussions, guidance, support, clear explanations, and original ideas. Moreover, for the inspiring atmosphere he created throughout my work. His patience and encouragement help the preparation of this dissertation. I am especially thankful for the intellectual freedom and motivation he provided, which greatly contributed to both my professional and personal development.

I would also like to thank Ádám Zlehovszky for his assistance with programming, for the many insightful explanations, and for the inspiring yet unanswerable questions that often opened new perspectives and ways of thinking.

Special thanks go to Csilla Pesznyák, who devoted an extraordinary amount of time and energy to the establishment of this program. Her persistent efforts and dedication made it possible for many of us to pursue our studies in this field.

I am deeply grateful to my wife, Júlia Andai, for her constant encouragement and unwavering support throughout the entire process. Her patience, understanding, and willingness to take on a significant share of our responsibilities greatly helped me in completing this dissertation. Without her support and sacrifices, this work would not have been possible.

Special thanks are due to my sons, Tamás Andai and Zoltán Lorenzó Andai, whose curiosity in exploring both the small and great connections of the world have been a constant source of inspiration to me. They still find wonder in countless things, and their thirst for knowledge seems inexhaustible. Their attitude and excitement for discovery influenced me as well, inspiring me to approach learning with renewed enthusiasm and joy.

I would also like to express my gratitude to my parents, who, perhaps unknowingly, guided me toward the field of Medical Physics. During my childhood, my father, Árpád Andai, often shared stories from his work at the National Office of Measures, particularly about the calibration of radioactivity measuring instruments, while my mother, Marianna Kovács, spoke about her experiences working as a nurse in the hospital.

Introduction

The present thesis is concerned with the mathematical and computational investigation of two-dimensional SPECT image reconstruction, with particular emphasis on the evolution of Fourier-domain characteristics during iterative reconstruction procedures.

The first section provides an overview of the fundamental principles of SPECT imaging. A schematic description of SPECT is presented, with particular emphasis on the role of the collimator, whose blurring effect is inherently distance-dependent. Furthermore, the mathematical framework of image reconstruction is introduced, including a discussion of the Maximum Likelihood Expectation Maximization (MLEM) reconstruction algorithm.

The second section focuses on the theory of one- and two-dimensional continuous and discrete Fourier transforms. Special attention is devoted to the relationship between the output of the Discrete Fourier Transform (DFT) algorithm and the coefficients of the trigonometric product terms ($\sin \times \sin$, $\sin \times \cos$, $\cos \times \sin$, and $\cos \times \cos$) arising in two-dimensional Fourier series expansions. In addition, this section contains a very mathematical and historical overview of the Gibbs phenomenon.

The third section presents in detail the modelling framework and the Python-based simulation environment developed for the investigation of two-dimensional SPECT imaging. This includes the precise geometrical configuration of the system, the algorithms used throughout the analyses, and a description of an artificial phantom, used during the initial testing phase.

The fourth section contains the principal results of the thesis. For the measurements performed on the different phantoms, the first one hundred images obtained during the iterative reconstruction process were studied from the perspective of Fourier analysis. The primary objective was to investigate how, and in what manner, the various Fourier coefficients converge to the corresponding Fourier coefficients of the original phantom as the iteration number increases.

The fifth section serves as an outlook and discusses several additional phantom families that were developed during the course of the research. Furthermore, it outlines a number of prospective mathematical analyses that could be carried out on the reconstructed datasets in future work.

1 SPECT

Single Photon Emission Computed Tomography (SPECT) is a medical imaging technique used in nuclear medicine to provide information about the function of organs and tissues. It is based on the use of radioactive tracers and tomographic image reconstruction methods. Similar to positron emission tomography (PET), SPECT images reflect functional processes in the body rather than only anatomical structures. SPECT and planar scintigraphy account for almost 80% of all nuclear medicine scans performed worldwide [6].

A SPECT scan is a type of nuclear imaging test that shows how blood flows to tissues and organs. In this technique, a radioactive-labeled pharmaceutical, known as a radiopharmaceutical, is administered to the patient. Depending on its distribution properties, the tracer accumulates in specific organs or tissue types. SPECT radiopharmaceuticals are based on gamma-emitting radioisotopes, such as ^{99m}Tc, ^{123}I, ^{131}I, ^{111}In, ^{67}Ga, ^{201}Tl, ^{81m}Kr, ^{133}Xe. These radionuclides emit gamma rays in the patient's body and that single photons can be detected by rotating detectors. These detectors move around the patient and record the emitted radiation from different angles. A scintillation detector is typically used as an imaging device. The schematic structure of the detector is shown in Figure 1. It consists of a lead collimator, which allows photons traveling in certain directions to pass through, and a scintillator crystal, which converts gamma-ray energy into light photons. These light photons are then converted into electrical signals by photomultiplier tubes (PMTs). Electronic circuits process these signals to determine the position where each photon interacts with the detector.

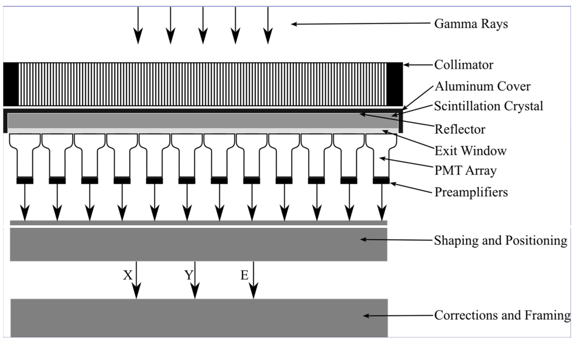

Figure 1: Schematic diagram about SPECT data acquisition.

The collected data are used by a computer to generate images. Initially, two-dimensional cross-sectional images are formed from the detected gamma rays. These cross-sections can then be combined to reconstruct a three-dimensional image, also called a sinogram, representing the distribution of the radiopharmaceutical within the body. In this work, we focus on the reconstruction of cross-sections, that is, to reconstruct 2D slices from the data.

1.1 Collimator

A SPECT collimator is a special metal grid between the patient and the gamma camera that filters out scattered gamma rays and allows only those travelling in specific directions to reach the detector. Only a small fraction (typically $10^{-4} - 10^{-2}$) of the emitted photons pass through the holes and are detected, which seriously limits sensitivity.

There is a so called resolution-sensitivity trade-off:
– bigger collimator holes increase the sensitivity and lower the resolution;
– smaller collimator holes decrease the sensitivity and increase the resolution.

Moreover, the resolution-sensitivity trade-off depends on:
– the size of the region of interest (ROI);
– the organs being imaged;
– the type of collimator;
– the energy of the emitted gamma rays;
– the detector's intrinsic spatial resolution;
– the size of the detector;
– the radius of rotation (ROR).

Ideally, collimator septa should block all incident radiation. In a real collimator a small percentage of radiation can penetrate the septa or can scatter off the septa itself. Since septal penetration and scatter increases with energy, collimators are designed usually for energy ranges.

The spatial resolution is an important system property and is expressed as the full-width-at-half-maximum (FWHM) of the point spread function (PSF), which is determined by the detector intrinsic resolution and the geometrical resolution of the collimator. The fundamental tradeoff between resolution and efficiency/sensitivity for parallel hole collimators is the following approximation.

$$(\text{FWHM resolution})^2 \approx \text{efficiency}$$

The spatial resolution is a combination of the intrinsic and the collimator response, which can be written as

$$\text{FWHM}_{\text{total}} = \sqrt{\text{FWHM}^2_{\text{intrinsic}} + \text{FWHM}^2_{\text{collimator}}}. \tag{1}$$

For parallel hole

$$\text{FWHM}_{\text{collimator}} = \frac{d}{L}x + \frac{d(L+B)}{L} \tag{2}$$

holds, where
x: distance between point source and collimator;
d: septa width, L: width of the collimator;
B: distance between the collimator and the image plane.

The normal distribution $N(\mu, \sigma)$ has a probability density function

$$f(x) = \frac{1}{\sqrt{2\pi}\sigma} \exp\left(-\frac{(x-\mu)^2}{2\sigma^2}\right).$$

It takes it's half maximum value at points $x_{1,2} = \mu \pm \sigma\sqrt{\log 4}$, leading to the

$$\mathrm{FWHM} = 2\sigma\sqrt{\log 4} \approx 2.35482\sigma$$

connection between σ and FWHM.

This means that according to Equations (1, 2), the spatial resolution can be written in the form of

$$\sigma_{\text{total}} = \sqrt{\sigma_{\text{int}}^2 + (\sigma_A x + \sigma_B)^2}.$$

1.2 Estimation of the pharmaceutical distribution

In modelling radioactive material, the most important distribution is the Poisson distribution. It is a discrete probability distribution with one parameter $\lambda > 0$. A discrete random variable X, in our case the number of emitted gamma rays, has a Poisson distribution if for every $n \in \mathbb{N}$

$$P(X = n) = \mathrm{e}^{-\lambda}\,\frac{\lambda^n}{n!}.$$

The Poisson distribution with parameter λ has mean λ and variance λ.

The image reconstruction algorithm used is based on the following mathematical framework.

1. The ROI is a finite square $[a,b]^2 \subseteq \mathbb{R}^2$, discretized as a square lattice $(c_j)_{j\in J}$. The radionuclide density at lattice points will be denoted by $(u_j)_{j\in J}$ or simply by the vector $u \in \mathbb{R}^{|J|}$. (For simplification only one index is used.)
2. Assume that there are $1, 2, \ldots, n$ points in the space, where the emitted photons can be measured. For simplification define $I = \{1, 2, \ldots, n\}$ and we refer to I as detectors. The number of detected photons by the ith $(i \in I)$ detector is denoted by b_i.
3. The number of detected photons caused by random events (scatter or background radiation) is $(r_i)_{i\in I}$.
4. Assume that the distribution of the number of detected photons can be written in the form of
$$b_i = \mathrm{Poi}((Au)_i + r_i), \tag{3}$$
where $A = (A_{ij})_{(i,j)\in I\times J}$ is the so called system matrix, which contains only nonnegative elements.

The reconstruction problem is the following: how can one reconstruct $(u_j)_{j\in J}$ if all the other quantities in Equation (3) are known?

Let us define $(Au)_i + r_i$ for every $i \in I$, and vectors $b, r \in \mathbb{R}^{|I|}$ which have components $(b_i)_{i\in I}$ and $(r_i)_{i\in I}$. The probability that b is the outcome of the measurement if u and r were the real values is the following.

$$P(b|u,r) = \prod_{i\in I} \exp\left(-(Au)_i - r_i\right) \frac{((Au)_i + r_i)^{b_i}}{b_i!}$$

The problem is that the number of emitted photons $(z_j)_{j\in J}$ at points $(c_j)_{j\in J}$ is unknown, it is a latent variable. One frequently used iterative method when data contains latent variable was presented by Dempster, Laird and Rubin in 1977 [2], it is called the Maximum Likelihood Expectation Maximisation (MLEM) method. The method was first applied to image reconstruction for emission tomography by Shepp and Vardi [8] in 1982. In the current setting, the method iterates the following two steps starting from the initial point $u^{(0)}$.

Expectation step (E-step): $\boxed{\text{Compute } Q(u|u^{(k)}) = \mathbb{E}_{z|b,u^{(k)}}\left(\log p(b,y|u)\right).}$

Maximisation Step (M-step): $\boxed{\text{Define } u^{(k+1)} = \arg\max_u Q(u|u^{(k)}).}$

In this situation the MLEM method leads to the following iteration.

$$u_j^{(k+1)} = \frac{u_j^{(k)}}{\sum_{i\in I} A_{ij}} \sum_{i\in I} A_{ij} \frac{b_i}{(Au^{(k)})_i + r_i} \tag{4}$$

The term $(Au^{(k)})_i + r_i$ is the E step, it determines the relative difference between the estimated and measured projections in order to update the current activity distribution toward the solution. The term $u_j^{(k)} \sum_{i\in I} A_{ij} \frac{b_i}{(Au^{(k)})_i + r_i}$ is the M step, it determines the relative difference between the estimated and measured projections to move the current activity distribution to be closer to the solution.

The convergence of the MLEM iteration is guaranteed by the following theorem [10, 8].

Theorem. If the initial estimate of the activity distribution $u^{(0)}$ $(\mathbb{R}^+)^{|J|}$, then for all $k \in \mathbb{N}$ we have

$$P(b|Au^{(k)} + r) \leq P(b|Au^{(k+1)} + r),$$

that is the likelihood does not decrease for the next estimate. The sequence $(u^{(k)})_{k\in\mathbb{N}}$ is converges and the limit $u = \lim_{k\to\infty} u^{(k)}$ has the following property.

$$\forall u' \in \left(\mathbb{R}^+\right)^{|J|}: \qquad P(b|Au' + r) \leq P(b|Au + r)$$

2 Fourier transform

The Gibbs phenomenon and later-used image analysis methods are also related to the Fourier transform. In this section, we briefly review the fundamentals of the Fourier transform, more precisely, the Fourier coefficients and Fourier series of continuous functions with unit period, their discretized version, and their two-dimensional generalisation.

2.1 1d Fourier transform

Let us begin with a 1-periodic, integrable function $f : \mathbb{R} \to \mathbb{R}$. By periodicity, it suffices to consider the fundamental domain $[0,1]$. The Fourier coefficients a_0, $(a_k)_{k\in\mathbb{N}^+}$, and $(b_k)_{k\in\mathbb{N}^+}$ represent, respectively, the mean value of f and the amplitudes of the cosine and sine modes at frequency $k \in \mathbb{N}^+$. They arise from projection f onto the orthonormal system

$$1, \quad \left\{\frac{1}{\sqrt{2}}\cos(2\pi kx)\right\}_{k\in\mathbb{N}^+}, \quad \left\{\frac{1}{\sqrt{2}}\sin(2\pi kx)\right\}_{k\in\mathbb{N}^+}, \tag{5}$$

which system is complete in the space of continuous functions with unit period. The Fourier coefficients are the following for $k \in \mathbb{N}^+$.

$$\begin{aligned} a_0 &= \int_0^1 f(x)\,\mathrm{d}\,x \\ a_k &= \int_0^1 f(x)\cos(2\pi kx)\,\mathrm{d}\,x \\ b_k &= \int_0^1 f(x)\sin(2\pi kx)\,\mathrm{d}\,x \end{aligned}$$

Using these coefficients, one constructs the N-th partial Fourier sum $S_N^{(f)}(x)$, which provides a trigonometric polynomial approximation of f.

$$S_N^{(f)}(x) = a_0 + 2\sum_{k=1}^{N}\left(a_k\cos(2\pi kx) + b_k\sin(2\pi kx)\right)$$

One can define its limit as

$$\tilde{f}(x) = a_0 + 2\sum_{k=1}^{\infty}\left(a_k\cos(2\pi kx) + b_k\sin(2\pi kx)\right) \tag{6}$$

for those $x \in \mathbb{R}$, where the series is convergent. When the limit exists, the function $\tilde{f}(x)$ denotes the Fourier series of f. The relationship between f and $\tilde{f}$ has an enormous literature. We just note here that its convergence properties depend on the regularity of f, and in particular, discontinuities lead to non-uniform convergence phenomena.

2.2 Discretized 1d Fourier transform

For computational purposes, the continuous setting is replaced by a discrete one. We divide the interval $[0,1]$ into $n = 2^p$ equidistant points, which is optimal for the Fast Fourier Transform (FFT). In this setting a general function is given on that finite set of equidistant points

$$f : \left\{0, \frac{1}{n}, \dots, \frac{n-1}{n}\right\} \to \mathbb{R}.$$

This discretization replaces integrals by finite sums and continuous frequencies by discrete modes. Introducing $q = \frac{2\pi}{n}$, the Discrete Fourier Transform (DFT) maps the sampled values of f to the complex coefficients

$$F_k = \mathrm{DFT}(f)_k = \sum_{x=0}^{n-1} f\left(\frac{x}{n}\right) \mathrm{e}^{-\mathrm{i}\,qkx}$$

for $k = 0, 1, \dots, n-1$. These coefficients encode both amplitude and phase information. The Inverse DFT (IDFT) for $x \in \left\{0, \frac{1}{n}, \dots, \frac{n-1}{n}\right\}$ is given as

$$g(x) = \mathrm{IDFT}(F)(x) = \sum_{k=0}^{n-1} F_k\, \mathrm{e}^{\mathrm{i}\,qkx}\,.$$

That is, for every function $f : \left\{\frac{0}{n}, \frac{1}{n}, \dots, \frac{n-1}{n}\right\} \to \mathbb{C}$ and $F : \{0, 1, \dots, n-1\} \to \mathbb{C}$

$$\mathrm{IDFT}(\mathrm{DFT}(f)) = f \quad \mathrm{DFT}(\mathrm{IDFT}(F)) = F$$

holds.

To connect the complex exponential formulation with the classical trigonometric form, one exploits symmetry properties of the coefficients. By pairing terms $F(k)$ and $F(n-k)$ using Euler's formula, the exponential representation can be rewritten in terms of sine and cosine functions.

$$\begin{aligned}
g(x) &= \sum_{k=0}^{n-1} F_k\, \mathrm{e}^{\mathrm{i}\,qkx} \\
&= F_0 + F_{n/2}\, \mathrm{e}^{\mathrm{i}\,\pi x} + \sum_{k=1}^{n/2-1} F_k\, \mathrm{e}^{\mathrm{i}\,qkx} + F_{n-k}\, \mathrm{e}^{-\mathrm{i}\,qkx} \\
&= F_0 + F_{n/2}\, \mathrm{e}^{\mathrm{i}\,\pi x} + \sum_{k=1}^{n/2-1} \mathrm{Re}(F_k + F_{n-k}) \cos(qkx) + \mathrm{Im}(-F_k + F_{n-k}) \sin(qkx)
\end{aligned}$$

So the classical Fourier coefficients are for $k = 1, 2, \dots, \frac{n}{2} - 1$

$$\begin{aligned}
a_0 &= F_0, & a_k &= \mathrm{Re}(F_k + F_{n-k})), & a_{n/2} &= F_{n/2} \\
b_0 &= 0, & b_k &= -\mathrm{Im}(F_k) + \mathrm{Im}(F_{n-k}), & b_{n/2} &= 0
\end{aligned}$$

and in this setting

$$g(x) = a_0 + a_{n/2}\,\mathrm{e}^{\mathrm{i}\,\pi x} + \sum_{k=1}^{n/2-1} a_k \cos(qkx) + b_k \sin(qkx)\,.$$

The terms are easy to interpret:
– a_0 is a constant shift;
– $a_{n/2}$ is the amplitude of the highest frequency $n/2$, where only the cos function occurs;
– the other terms are usual Fourier factors.
Note that $g(x) = f(x)$ holds for every $x \in \left\{\frac{0}{n}, \frac{1}{n}, \ldots, \frac{n-1}{n}\right\}$.

2.3 2d Fourier transform

The extension to two dimensions follows a tensor-product structure. For an integrable $f : \mathbb{R}^2 \to \mathbb{R}$ function with period $(1,0)$ and $(0,1)$, the Fourier expansion consists of products of sine and cosine functions in the first and second variable. The coefficients describe interactions between frequencies in each direction. The coefficients are the following for every $k, l \in \mathbb{N}^+$.

$$\begin{aligned}
a_0 &= \int_0^1 \int_0^1 f(x,y)\,\mathrm{d}\,x\,\mathrm{d}\,y \\
ac_{k0} &= \int_0^1 \int_0^1 f(x,y)\cos(2k\pi x)\,\mathrm{d}\,x\,\mathrm{d}\,y \\
as_{k0} &= \int_0^1 \int_0^1 f(x,y)\sin(2k\pi x)\,\mathrm{d}\,x\,\mathrm{d}\,y \\
ac_{0l} &= \int_0^1 \int_0^1 f(x,y)\cos(2l\pi y)\,\mathrm{d}\,x\,\mathrm{d}\,y \\
as_{0l} &= \int_0^1 \int_0^1 f(x,y)\sin(2l\pi y)\,\mathrm{d}\,x\,\mathrm{d}\,y \\
\alpha_{kl} &= \int_0^1 \int_0^1 f(x,y)\cos(2k\pi x)\cos(2l\pi y)\,\mathrm{d}\,x\,\mathrm{d}\,y \\
\beta_{kl} &= \int_0^1 \int_0^1 f(x,y)\sin(2k\pi x)\sin(2l\pi y)\,\mathrm{d}\,x\,\mathrm{d}\,y \\
\gamma_{kl} &= \int_0^1 \int_0^1 f(x,y)\sin(2k\pi x)\cos(2l\pi y)\,\mathrm{d}\,x\,\mathrm{d}\,y \\
\delta_{kl} &= \int_0^1 \int_0^1 f(x,y)\cos(2k\pi x)\sin(2l\pi y)\,\mathrm{d}\,x\,\mathrm{d}\,y
\end{aligned}$$

From these Fourier coefficients one can define the Fourier sum

$$\begin{aligned} g(x,y) =& a_0 + 2\sum_{k=1}^{N} ac_{k0}\cos(2k\pi x) + as_{k0}\sin(2k\pi x) \\ &+ 2\sum_{l=1}^{M} ac_{0l}\cos(2k\pi y) + as_{0l}\sin(2k\pi y) \\ &+ 4\sum_{k,l=1}^{N,M}\Big(\alpha_{kl}\cos(2k\pi x)\cos(2l\pi y) + \beta_{kl}\sin(2k\pi x)\sin(2l\pi y) \\ &\qquad + \gamma_{kl}\sin(2k\pi x)\cos(2l\pi y) + \delta_{kl}\cos(2k\pi x)\sin(2l\pi y)\Big). \end{aligned}$$

If the function f is smooth enough (for example twice continuously differentiable), then the Fourier sum reproduces f, that is $g = f$.

2.4 Discretized 2d Fourier transform

In the discrete case, the two-dimensional DFT produces coefficients $F_{k,l}$. As before, assume that the unit square $[0,1]^2$ divided into $2^p \times 2^p$ equidistant points. In this setting a general function is given on that finite set of equidistant points

$$f : \left\{0, \frac{1}{n}, \ldots, \frac{n-1}{n}\right\}^2 \to \mathbb{R}.$$

Using the same notion $q = \frac{2\pi}{n}$, the discrete 2d Fourier transform maps f to complex coefficients

$$F_{k,l} = \mathrm{DFT}(f)_{k,l} = \sum_{x,y=0}^{n-1} f\left(\frac{x}{n}, \frac{y}{n}\right) \mathrm{e}^{-\mathrm{i}\, q(kx+ly)}$$

for $k, l = 0, 1, \ldots, n-1$. The IDFT for $x, y \in \left\{0, \frac{1}{n}, \ldots, \frac{n-1}{n}\right\}$ is given as

$$g(x,y) = \mathrm{IDFT}(F)(x,y) = \sum_{k,l=0}^{n-1} F_{k,l}\, \mathrm{e}^{\mathrm{i}\, q(kx+ly)}\,.$$

As before, for every function $f : \left\{\frac{0}{n}, \frac{1}{n}, \ldots, \frac{n-1}{n}\right\}^2 \to \mathbb{R}$ and $F : \{0, 1, \ldots, n-1\}^2 \to \mathbb{R}$ we have

$$\mathrm{IDFT}(\mathrm{DFT}(f)) = f \quad \mathrm{DFT}(IDFT(F)) = F.$$

By grouping symmetric terms, as in the 1d case, and separating real and imaginary parts, we can obtain a real-valued trigonometric expansion involving cosine–cosine, sine–sine, and mixed sine–cosine terms.

$$
\begin{aligned}
g(x,y) &= \sum_{k,l=0}^{n-1} F_{k,l}\, \mathrm{e}^{\mathrm{i}\, q(kx+ly)} = \sum_{l=0}^{n-1}\sum_{k=0}^{n-1} F_{k,l}\, \mathrm{e}^{\mathrm{i}\, q(kx+ly)} \\
&= \sum_{l=0}^{n-1} F_{0,l}\, \mathrm{e}^{\mathrm{i}\, qly} + F_{n/2,l}\, \mathrm{e}^{\mathrm{i}\, \pi x + \mathrm{i}\, qly} + \mathrm{e}^{\mathrm{i}\, qly} \sum_{k=1}^{n/2-1} \left(F_{k,l}\, \mathrm{e}^{\mathrm{i}\, qkx} + F_{n-k,l}\, \mathrm{e}^{-\mathrm{i}\, qkx} \right) \\
&= F_{0,0} + F_{n/2,0}\, \mathrm{e}^{\mathrm{i}\, \pi x} + \sum_{k=1}^{n/2-1} \left(F_{k,0}\, \mathrm{e}^{\mathrm{i}\, qkx} + F_{n-k,0}\, \mathrm{e}^{-\mathrm{i}\, qkx} \right) \\
&\quad + F_{0,n/2}\, \mathrm{e}^{\mathrm{i}\, \pi y} + F_{n/2,n/2}\, \mathrm{e}^{\mathrm{i}\, \pi x + \mathrm{i}\, \pi y} + \mathrm{e}^{\mathrm{i}\, \pi y} \sum_{k=1}^{n/2-1} \left(F_{k,n/2}\, \mathrm{e}^{\mathrm{i}\, qkx} + F_{n-k,n/2}\, \mathrm{e}^{-\mathrm{i}\, qkx} \right) \\
&\quad + \sum_{l=1}^{n/2-1} \left(F_{0,l}\, \mathrm{e}^{\mathrm{i}\, qly} + F_{0,n-l}\, \mathrm{e}^{-\mathrm{i}\, qly} + F_{n/2,l}\, \mathrm{e}^{\mathrm{i}\, \pi x + \mathrm{i}\, qly} + F_{n/2,n-l}\, \mathrm{e}^{\mathrm{i}\, \pi x - \mathrm{i}\, qly} \right) \\
&\quad + \sum_{k,l=1}^{n/2-1} \left(F_{k,l}\, \mathrm{e}^{\mathrm{i}\, q(kx+ly)} + F_{n-k,l}\, \mathrm{e}^{\mathrm{i}\, q(-kx+ly)} + F_{k,n-l}\, \mathrm{e}^{\mathrm{i}\, q(kx-ly)} + F_{n-k,n-l}\, \mathrm{e}^{\mathrm{i}\, q(-kx-ly)} \right)
\end{aligned}
$$

This expansion lead us to define

$$
a_{0,0} = F_{0,0}, \quad a_{n/2,0} = F_{n/2,0} \quad a_{0,n/2} = F_{0,n/2}, \quad a_{n/2,n/2} = F_{n/2,n/2}
$$

and for all $1 \le k,l \le n/2-1$ integer values

$$
\begin{aligned}
a_{k,0} &= \mathrm{Re}(F_{k,0} + F_{n-k,0}), & b_{k,0} &= \mathrm{Im}(-F_{k,0} + F_{n-k,0}) \\
a_{0,l} &= \mathrm{Re}(F_{0,l} + F_{0,n-l}), & b_{0,l} &= \mathrm{Im}(-F_{0,l} + F_{0,n-l}) \\
a_{k,n/2} &= \mathrm{Re}(F_{k,n/2} + F_{n-k,n/2}), & b_{k,n/2} &= \mathrm{Im}(-F_{k,n/2} + F_{n-k,n/2}) \\
a_{n/2,l} &= \mathrm{Re}(F_{n/2,l} + F_{n/2,n-l}), & b_{n/2,l} &= \mathrm{Im}(-F_{n/2,l} + F_{n/2,n-l})
\end{aligned}
$$

moreover for all $1 \le k,l \le n/2-1$ integer values

$$
\begin{aligned}
\alpha_{k,l} &= \mathrm{Re}\left(F_{k,l} + F_{n-k,n-l} + F_{n-k,l} + F_{k,-l}\right) \\
\beta_{k,l} &= \mathrm{Re}\left(-F_{k,l} - F_{n-k,n-l} + F_{n-k,l} + F_{k,n-l}\right) \\
\gamma_{k,l} &= \mathrm{Im}\left(-F_{k,l} + F_{n-k,n-l} + F_{n-k,l} - F_{k,n-l}\right) \\
\delta_{k,l} &= \mathrm{Im}\left(-F_{k,l} + F_{n-k,n-l} - F_{n-k,l} + F_{k,n-l}\right).
\end{aligned}
$$

Using these coefficients the Fourier series can be written as

$$
\begin{aligned}
g(x,y) &= a_{0,0} + a_{n/2,0}\,\mathrm{e}^{\mathrm{i}\,\pi x} + a_{0,n/2}\,\mathrm{e}^{\mathrm{i}\,\pi y} + a_{n/2,n/2}\,\mathrm{e}^{\mathrm{i}\,\pi(x+y)} \\
&+ \sum_{k=1}^{n/2-1} a_{k,0}\cos(qkx) + b_{k,0}\sin(qkx) + \sum_{l=1}^{n/2-1} a_{0,l}\cos(qly) + b_{0,l}\sin(qly) \\
&+ \mathrm{e}^{\mathrm{i}\,\pi y} \sum_{k=1}^{n/2-1} a_{k,n/2}\cos(qkx) + b_{k,n/2}\sin(qkx) \\
&+ \mathrm{e}^{\mathrm{i}\,\pi x} \sum_{l=1}^{n/2-1} a_{n/2,l}\cos(qly) + p_{n/2,l}\sin(qly) \\
&+ \sum_{k,l=1}^{n/2-1} \Big(\alpha_{kl}\cos(qkx)\cos(qly) + \beta_{kl}\sin(qkx)\sin(qly) \\
&\qquad + \gamma_{kl}\sin(qkx)\cos(qly) + \delta_{kl}\cos(qkx)\sin(qly)\Big).
\end{aligned}
$$

From this calculation it can also be seen that in two dimensions there are more Fourier coefficients, and their role is less visually apparent than in one dimension. It is important to highlight the four *Fourier matrices* $(\alpha_{k,l}, \beta_{k,l}, \gamma_{k,l}, \delta_{k,l})$, which encode the amplitudes of the different modes coupled along the x and y coordinates.

2.5 Gibbs phenomenon

Albert Michelson built a mechanical device in 1898, named a Harmonic Analyzer, that stored the Fourier coefficients of a given curve in its springs. For visualisation see the youtube video *An Old Mechanical Computer: The Harmonic Analyzer* [3] or for more details the book [5] by Hammack, Kranz, and Carpenter. Lanczos [7, p. 51] claimed that Michelson was puzzled by the fact that he could not reconstruct the square wave function and posed the problem to his friend J. Willard Gibbs. In 1899 Gibbs proved that no matter how many oscillations are taken into account to reconstruct a square wave, the overshoot tends to a fixed number [4]. This result was referred by Bôcher in 1906 as Gibbs phenomenon [1].

The Figure 2 illustrates what happens when we try to approximate a square wave using harmonic functions. It can be seen that using 5, 50, or 500 harmonics results in an increasingly accurate approximation of the square wave; however, in each case, an overshoot appears at the discontinuities of the square wave.

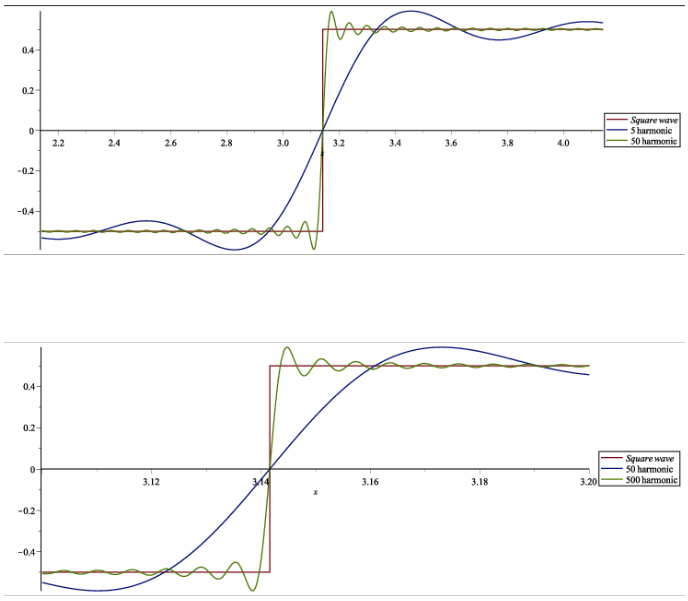

Figure 2: Gibbs effect.

In this case, the square wave has a unit jump at π. The magnitude of the jump can be defined mathematically in the following way. Let S_n denote the n-th partial sum of the Fourier series of the square wave. Define $x_n = \min\{x \in]\pi, \infty[\, |S_n'(x) = 0\}$, that is where S_n has the first local maximum after the jump. The limit

$$G = \lim_{n\to\infty} S_n(x_n).$$

exists, moreover it can be computed explicitly

$$G = \frac{1}{2} + \frac{1}{\pi}\int_0^\pi \frac{\sin t}{t}\,dt \approx 1.08948987.$$

This constant quantifies the overshooting effect in one dimension. The overshoot is directly proportional to the amplitude of the jump, so in one dimension it is approximately 9%.

It is important to note that this phenomenon is a consequence of the discontinuity of the underlying function. If one considers a function with a very steep but continuous transition, for example,

$$f : [0,1] \to \mathbb{R} \qquad x \mapsto \begin{cases} 0, & \text{if } 0 \le x < \frac{1}{2}, \\ \frac{2x-1}{2a}, & \text{if } \frac{1}{2} \le x < \frac{1}{2} + a, \\ 1, & \text{if } \frac{1}{2} + a \le x < 1 - a, \\ \frac{1-x}{a}, & \text{if } 1 - a \le x \le 1, \end{cases}$$

where $a \in \left]0, \frac{1}{4}\right[$ is a parameter, then for any arbitrarily small $\varepsilon > 0$ (because of the Weierstrass approximation theorem) there exists a trigonometric polynomial

$$T(x) = q_0 + \sum_{k=0}^{N} q_n \cos(nx) + w_n \sin(nx), \text{ such that for all } x \in [0,1]$$

$$|f(x) - T(x)| < \varepsilon$$

holds. The mentioned Weierstrass approximation theorem is about that every continuous periodic function can be approximated uniformly by trigonometric polynomials with arbitrarily small error.

To understand how behaves the overshoot of the Fourier series in higher dimensions, it is enough to examine the two-dimensional case. In two dimensions, an important observation is that

$$L^2\left([0,1]^2, \mathbb{R}\right) = L^2([0,1], \mathbb{R}) \otimes L^2([0,1], \mathbb{R})$$

that is, the space can be expressed as the tensor product of one-dimensional function spaces.

Let $(e_n)_{n\in\mathbb{N}}$ denote the complete orthonormal system of $L^2([0,1], \mathbb{R})$ given by Equation (5). Then the system $(e_i \otimes e_j)_{i,j\in\mathbb{N}}$ forms a complete orthonormal system in $L^2\left([0,1]^2, \mathbb{R}\right)$.

Consider the function

$$f : [0,1]^2 \to \mathbb{R} \qquad (x,y) \mapsto \begin{cases} 1, & \text{if } x > \frac{1}{2} \text{ and } y > \frac{1}{2}, \\ 0, & \text{otherwise.} \end{cases}$$

Due to the symmetry of the variables and the tensor product structure of the space, the two-dimensional Fourier series of f can be written as the product of two one-dimensional Fourier series. More precisely, let

$$g : [0,1] \to \mathbb{R} \qquad (x) \mapsto \begin{cases} 1, & \text{if } x > \frac{1}{2}, \\ 0, & \text{otherwise,} \end{cases}$$

and denote its Fourier series by $\tilde{g}$. (See Equation (6) for definition.) Then the Fourier series of f is given by

$$\tilde{f}(x,y) = \tilde{g}(x) \times \tilde{g}(y).$$

Since the overshoot along each coordinate axis is G, the total overshoot in two dimensions is given by G^2.

The overshoot in two dimensions is approximately 19% (G^2) and in three dimensions 29% (G^3). This highlights an important practical limitation of Fourier-based approximations near discontinuities.

In mathematics, it often happens that a result is later found to have been discovered earlier, but it was published at the wrong time or in the wrong place, and therefore was forgotten. The fact that a discontinuous function can be represented as an infinite sum of sines and cosines was known already to Euler, who presented, in the middle of the 18th century, the following sum.

$$\forall x \in]0, 2\pi[: \qquad \frac{\pi - x}{2} = \sum_{n=1}^{\infty} \frac{\sin(nx)}{n}$$

The nonuniform convergence of the Fourier series for discontinuous functions, and in particular the oscillatory behaviour of the finite sum, was already analysed by Henry Wilbraham, who in 1848 published a result in which he even included a clear illustration of the Gibbs effect and also calculated the value of the constant G defined above [9].

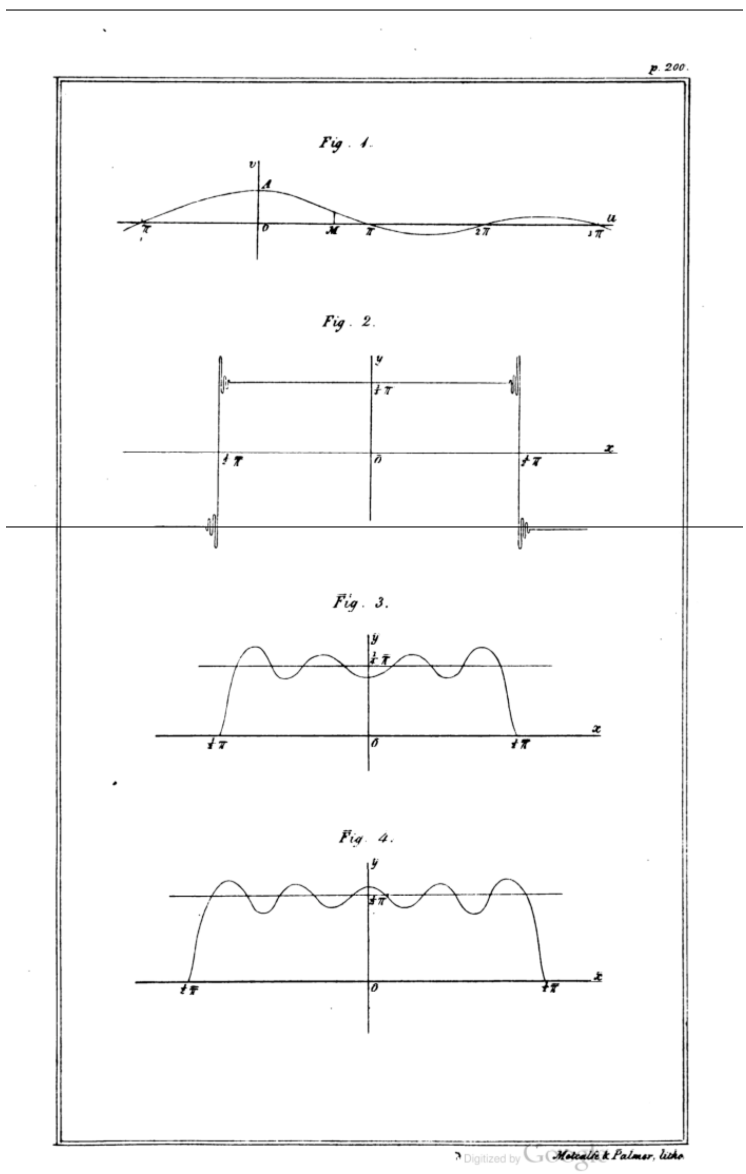

Figure 3: Wilbraham's illustration about Gibbs phenomenon in 1848.

3 Reconstruction program

In this section, the software developed as part of this research is presented, with particular emphasis on its role in implementing and analysing the MLEM iterative algorithm. The primary objective of the program is to provide a flexible and computationally efficient framework for executing the MLEM method, enabling both theoretical investigation and practical application within the scope of this study.

3.1 Main functions for the iterative image reconstruction

The program has modular structure. The most important modules is presented with explanations when it is necessary.

Description: Used libraries, modules and functions.

```
# importing required libraries
import numpy as np
from mpl_toolkits.mplot3d import Axes3D
import matplotlib.pyplot as plt
from scipy.ndimage import rotate
from scipy.ndimage import gaussian_filter
import scipy.fftpack
from skimage.transform import resize
import time
from tqdm import tqdm
import cv2
from dataclasses import dataclass
```

In the program the SPECT geometry visualised in Figure 4 was used. The region of interest (ROI) was defined as a square with a side length of 384 mm. All phantoms were confined within a circular domain of radius 271 mm, centred at the midpoint of the ROI. This geometric configuration simplifies the projection process, as it guarantees that, regardless of the ROI's rotation, the phantom remains entirely within the 384 mm field of the detector.

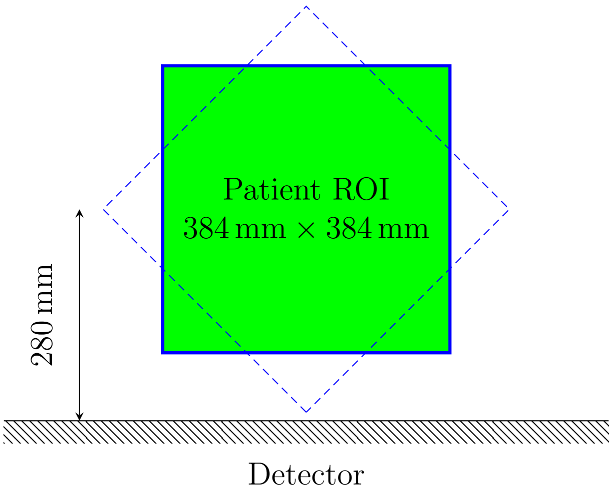

Figure 4: The SPECT geometry.

The ROI was discretized into a 256×256 square lattice. During data acquisition, the ROI was rotated over a full 360° range in increments of 3°. The system's spatial resolution was modelled using a full width at half maximum (FWHM) parametrisation, with $\mathrm{FWHM_{intrinsic}} = \sigma_{\mathrm{int}} = 1.5\,\mathrm{mm}$, and additional Gaussian components characterised by $\sigma_A = 0.6196\,\mathrm{mm}$ and $\sigma_B = 0.01835$.

Description: Default parameters and their values.

```
# Default values
DefPatientROISize_mm = 384
DetectorROICenter_mm = 280
Intrinsic_Sigma = 1.5
SigmaA = 0.6196
SigmaB = 0.01835

DefImgSize_px = 256
DefAngle = 3
DefMeasureTime = 1
Defnoiseamplitude = 300
DefPixelSize_mm = DefPatientROISize_mm / DefImgSize_px
np.random.seed(42)

NumOfAngles = int(360 / DefAngle)
angles_deg= np.linspace(0, 360, NumOfAngles)

epsilon = 1e-4
```

The effective FWHM, accounting for both intrinsic detector resolution and collimator effects, was modelled as

$$\sqrt{\sigma_{\mathrm{int}}^2 + (\sigma_A + \sigma_B x)^2},$$

where (x) denotes the distance from the detector in millimeters. In specific scenarios, a constant FWHM value of 2 mm was assumed. In other cases, blurring effects were neglected entirely, corresponding to an idealised setting in which the FWHM was set to 0 mm.

Objective:	Generate different kind of sigma values based on the coordinate for Gaussian filter.
Input:	coor: detectordistance_mm: the distance from the detector, num: type of sigma change
Output:	sigma value
Used:	in Gaussian filter

```
def GaussSigma(detectordistance_mm,num):
    if num == 1:
        sigma_mm = np.sqrt(Intrinsic_Sigma**2 + (SigmaA + SigmaB *
        ↪  detectordistance_mm)**2)
    elif num == 2:
        sigma_mm = 2
    else:
        sigma_mm = 0
    sigma_return = sigma_mm / DefPixelSize_mm
    return sigma_return
```

The following function implements distance-dependent blurring applied to the input image.

Objective:	Gaussian filter an image, where the sigma value changes line by line.
Input:	picmatrix: 2D image matrix, filterparam: how standard deviation depends on distance
Output:	filtered image matrix
Used:	projection

```
def GaussFilter_byline(picmatrix,filterparam):
    ww,hh = picmatrix.shape
    newpic = np.zeros((ww,hh))
    BottomofPicmatrix_mm = DetectorROICenter_mm - (ww / 2) * DefPixelSize_mm
    if BottomofPicmatrix_mm < 0:
        print("Warning: DetectorROICenter_mm is too small, negative detector
        ↪  distance occurs!")
        exit()
    for curlinenum in range(ww):
        detectordistance= BottomofPicmatrix_mm + curlinenum * DefPixelSize_mm
        sigmaC = GaussSigma(detectordistance,filterparam)
        curline = picmatrix[curlinenum,:]
        if sigmaC > 0:
            newcurline = np.zeros(len(curline))
```

```
            gaussian_filter(curline, sigma = sigmaC, mode = 'constant', truncate
            ↪  = 3.0, output = newcurline)
        else:
            newcurline = curline
        newpic[curlinenum,:] = newcurline
    return newpic
```

The following function (the Forward Projection (FP)) computes the discretized Radon transform. The input image is rotated according to the angles specified in the `anglelist` parameter. For each rotation, the image is convolved with a distance-dependent Gaussian kernel to model system blurring, and subsequently projected onto the horizontal axis by summing over the horizontal coordinates. The resulting set of projections forms the angle-projection sinogram.

Objective:	Coordinate dependent Gaussian filter and Radon transform.
Input:	imgparam: 2D image matrix, anglelist: list of angles, numparam: how standard deviation depends on distance
Output:	Radon transformed image matrix
Used:	in projection

```
def ForwardProjection(imgparam, anglelist, numparam):
    sinogram = []
    for angleparam in anglelist:
        rotated_imageparam = rotate(imgparam, angleparam, reshape = False, order
        ↪  = 1)
        imgfilteredparam = GaussFilter_byline(rotated_imageparam, numparam)
        projectionFilteredImage = np.sum(imgfilteredparam, axis = 0)
        sinogram.append(projectionFilteredImage)
    radon_image = np.stack(sinogram, axis = 0)
    return radon_image
```

In the forward projection step, the transformation applied to the image can be expressed as the composition

$$(\text{Projection} \circ \text{Blur} \circ \text{Rotate})(\text{Image}).$$

That is, the image is first rotated, then convolved with a distance-dependent blurring kernel, and finally projected onto the detector domain.

The backprojection (BP) step can be interpreted as the adjoint (inverse in some loose sense) of this process. In this case, the input is an angle-projection sinogram. For each projection angle, the corresponding one-dimensional projection is redistributed across the image domain along the associated projection paths, effectively reversing the projection operation. This intermediate result is then convolved with the same blurring model to ensure consistency with the forward operator, and subsequently rotated back to the original coordinate system.

The final reconstructed image is obtained by summing the contributions from all projection angles. This accumulation corresponds to the application of the transpose of the system operator, forming the backprojection component of the MLEM iteration.

Objective:	Backprojection with Gaussian filter.
Input:	Radon transformed picture, sizes of the original image, filter type
Output:	backprojected image
Used:	in reconstruction

```
def BackwardProjection(recdata, filterparam):
    anglenum = recdata.shape[0]
    defwidth = recdata.shape[1]
    bprojected = np.zeros((defwidth, defwidth))
    for preangle in range(anglenum):
        angle = 360 * preangle / anglenum
        tempprojected = np.zeros((defwidth, defwidth))
        for ee in range(defwidth):
            tempprojected[ee,:] = recdata[preangle,:]
        tempfiltered = GaussFilter_byline(tempprojected, filterparam)
        temprotated = rotate(tempfiltered, -angle, reshape=False, order=1)
        bprojected += temprotated
    return bprojected
```

This function generates a measurement based on an artificial phantom. First, the artificial phantom (imgpre) is rescaled to the required resolution of 256×256 pixels. Next, its forward projection is computed. The temporal effects is optional and is generally not applied. Finally, Poisson noise can be added to the resulting image to simulate the stochastic nature of radioactive decay.

Objective:	Create input image for the reconstruction.
Input:	an original image to reconstruct, filter type
Output:	recon input image with(out) Poisson noise
Used:	in reconstruction

```
def CreateReconInput(imgpre,num):
    img = resize(imgpre, (DefImgSize_px, DefImgSize_px))
    # Filter and back project
    szogek = DefAngle * np.arange(NumOfAngles)
    measurement = ForwardProjection(img, szogek, num)
    #measurement = DefMeasureTime * measurement # Optional!
    #measurement = np.random.poisson(measurement) # Optional!
    return measurement
```

The iterative reconstruction algorithm is based on the MLEM iteration formula.

$$u_j^{(k+1)} = \frac{u_j^{(k)}}{\sum_{i \in I} A_{ij}} \sum_{i \in I} A_{ij} \frac{b_i}{(Au^{(k)})_i + r_i}$$

Since the computation of the system matrix is computationally expensive and the reconstruction algorithm itself is also slow, an alternative approach was adopted.

The term $Au^{(k)} + r$ is replaced by a forward projection, to which a small regularisation parameter ε is added. This modification is necessary because the expression appears in the denominator, and zero or near-zero values may lead to numerical instabilities. Accordingly, the denominator is written as "ForwardProjection$(u^{(k)}) + \varepsilon$", which is sometimes denoted by $\text{Signal}^{(k)}$. The expression $\sum_{i \in I} A_{ij} \frac{b_i}{\text{Signal}_i^{(k)}}$ is computed via the backprojection of the ratio $\frac{b_i}{\text{Signal}_i^{(k)}}$. The normalisation factor for the backprojection, $\sum_{i \in I} A_{ij}$, is obtained by performing the backprojection of a sinogram with constant value 1. The normalisation constant for the backprojection is

Objective:	Reconstruction algorithm.
Input:	initial image, recon input, system matrix, image size, number of iterations, epsilon
Output:	list of reconstructed images
Used:	Reconstruct image

```
def Reconstruction_Iteration(imageini, measurement3, ImgSize, iternumber,
↪ Filtertype, varepsilon):
    norm2v = BackwardProjection(np.ones_like(measurement3,
     ↪ dtype=np.float32),Filtertype)
  + varepsilon
    reconiter = np.zeros((iternumber+1, ImgSize, ImgSize))
    reconiter[0,:,:] = imageini
    for current_iteration in tqdm(range(iternumber)):
        image_estimate2 = reconiter[current_iteration,:,:]
        signal2 = ForwardProjection(image_estimate2, angles_deg, Filtertype) +
         ↪ varepsilon
        ratio2 = measurement3 / signal2
        image_estimate2 *= BackwardProjection(ratio2, Filtertype) / norm2v
        reconiter[current_iteration+1,:,:] = image_estimate2
    return reconiter
```

3.2 Test Phantom and Its Reconstruction

The algorithm was first evaluated using a phantom. The test phantom is represent a cylinder with cold rods inside, it will be referred as cylindrical phantom. In

2 dimension the phantom is circular, with a higher activity level inside the disk. Within this region, n smaller circles are placed, with their centres located at the vertices of a regular n-gon. The activity within the smaller circles decreases according to an arithmetic progression, defined such that the (hypothetical) $n + 1$ circle would have an activity equal to that of the interior of the large circle.

This phantom can be generated using the following function.

Objective:	Create phantom image for testing.
Input:	relative radius of the big and small circles, activity values for different regions
Output:	2D phantom image matrix
Used:	An example object with hot/cold spots

```
def TestPhantom(Ngon,CircleRadius, Circleradius, ActivityBBG, ActivityBG,
↪ ActivityR):
    imagePhantom = np.zeros((DefImgSize_px, DefImgSize_px))
    imagePhantom += ActivityBBG
    R = DefImgSize_px/2*CircleRadius
    gonangle = 2*np.pi / Ngon
    ashift = R/(1+np.sin(gonangle/2))
    r=ashift*np.sin(gonangle/2)*Circleradius
    activitystep=(ActivityR-ActivityBG)/Ngon
    for ee in range(DefImgSize_px):
        for ff in range(DefImgSize_px):
            if ((ee-DefImgSize_px/2)**2+(ff-DefImgSize_px/2)**2)<R**2:
                imagePhantom[ff,ee] = ActivityBG
            for gg in range(Ngon):
                xc=DefImgSize_px/2+ashift*np.cos(gg*gonangle)
                yc=DefImgSize_px/2+ashift*np.sin(gg*gonangle)
                if ((ee-xc)**2+(ff-yc)**2)<r**2:
                    imagePhantom[ff,ee] = ActivityBG + (gg+1)*activitystep
    return imagePhantom
```

The case shown below corresponds to five smaller circles and the following activity values. Outside the large circle, there is a colder (lower-activity) region with an activity value of 0.2, while inside the large circle there is a hotter (higher-activity) region with an activity value of 1, and activity of the coldest small circle is 0.5.

The phantom and the first reconstruction was done by the following code.

```
DefPhantomCircleRadius = 0.7
DefPhantomCircleradius = 0.6
DefActivityBBG = 0.2
DefActivityBG = 1
```

```
DefActivityR = 0.5
RelativeRadiusInitialImage = 0.9
DefNumberOfSmallCircles = 5

Filtertype = 1 # 1: coordinate dependent Gaussian filter, 2: constant, 0: no
↪  filter

image = 100*TestPhantom(DefNumberOfSmallCircles, DefPhantomCircleRadius,
↪  DefPhantomCircleradius, DefActivityBBG, DefActivityBG, DefActivityR)
sinogram = ForwardProjection(image, angles_deg, Filtertype)
measurement = np.random.poisson(sinogram)
backprojected=BackwardProjection(sinogram, Filtertype)
InitialImage = CreateReconInitialImage(measurement,RelativeRadiusInitialImage)

norm2 = BackwardProjection(np.ones_like(measurement, dtype=np.float32),1) +
↪  epsilon

iternumber = 100
iterrec = Reconstruction_Iteration(image_estimate2, measurement, DefImgSize_px,
↪  iternumber, Filtertype,epsilon)
```

The phantom and it's sinogram presented in Figure 5a and 5b.

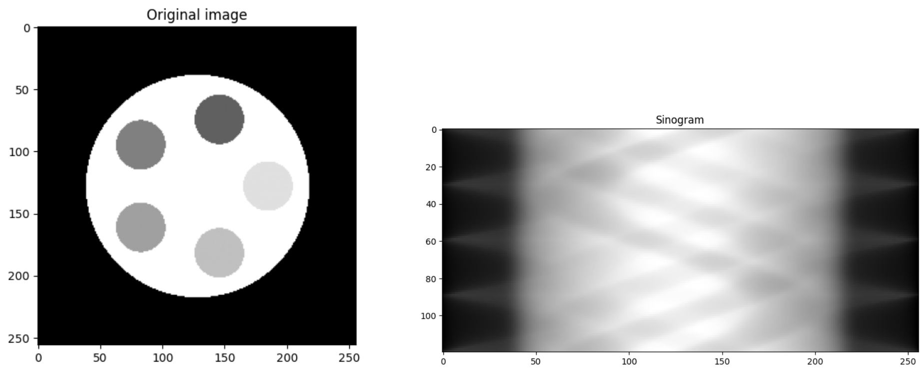

(a) Original image. (b) Sinogram.

Figure 5: A forward projection.

The first backprojection, it's normalisation and the result after 100 reconstruction iteration can be seen in Figure 6.

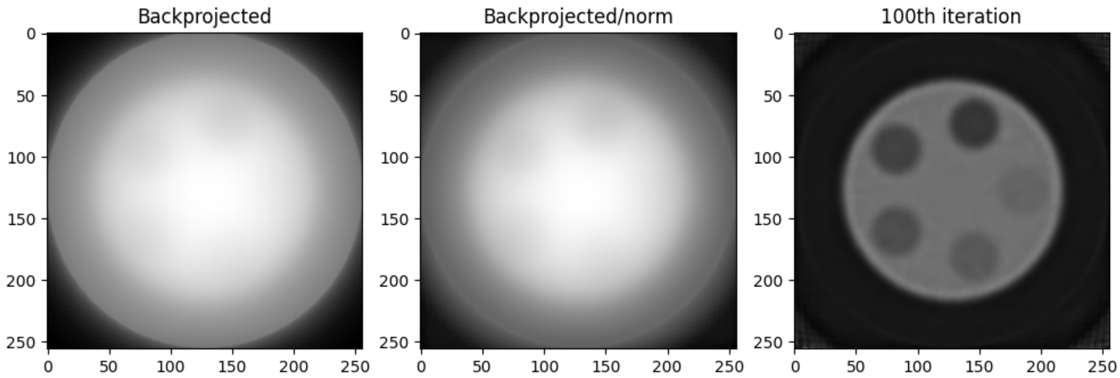

Figure 6: Test phantom and it's reconstruction.

4 Phantoms

This section is about the behaviour of the Fourier components of the iterated images with respect to the phantom. A detailed study is then carried out on the evolution of the two-dimensional Fourier coefficients of the reconstructed images as a function of the iteration number. The convergence properties of the four Fourier matrices are analysed one by one, to give insight their behaviour. Beyond the individual matrices, the convergence behaviour of the corresponding Fourier hypermatrix (whose elements are four-dimensional vectors composed of the Fourier matrix components) is also investigated. This could provide a more comprehensive description of the multidimensional convergence structure arising during the iterative reconstruction process.

In addition, the section introduces another class of test objects, referred to as the sectoral phantom family. Using this phantom family, the reconstruction performance after 100 iterations is evaluated for a range of phantom parameter configurations. The analysis focuses on how accurately the associated Fourier matrices can be recovered depending on the geometric and structural properties of the phantom.

4.1 Cylindrical phantom

4.1.1 Gibbs effect at a section

At cylindrical phantom, with resolution 256×256 the row 170 was selected for the study of the Gibbs effect. Figure 7 show the 1 dimensional cross section of the cylindrical phantom at row 170 and it's reconstruction. It provides a clear visual demonstration of the Gibbs phenomenon.

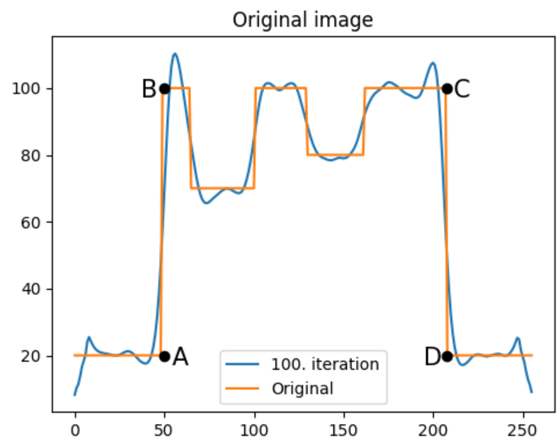

Figure 7: Cross section of the cylindrical phantom and it's reconstruction at row 170.

At the first upward discontinuity ($\overrightarrow{AB}$), an overshoot is observed in the reconstructed signal and a similar effect can be identified just before the final downward ($\overrightarrow{CD}$) jump, where the signal again overshoots prior to transitioning to the lower level.

Corresponding undershoot can be observed near points A and D. However, in this case, the undershoot is less significant than the overshoot. The magnitude of the overshoot at the first upward jump is notably large. It may be caused by the fact the original function has elevated plateau over a relatively short interval (approximately between indices 50 and 60) and expected overshoots at both edges overlap. This superposition could effectively amplify the observed overshoot and lead to a more prominent artifact.

In contrast, the overshoot preceding the final downward jump occurs in a region where the signal maintains a higher value over a longer interval. This allows the oscillatory behaviour to develop more independently of neighbouring discontinuities, yielding a more classical manifestation of the Gibbs phenomenon.

Figure 8 show the two previously identified overshoots normalised to unit magnitude at each iteration, and the corresponding overshoot amplitudes are plotted as a function of the iteration count.

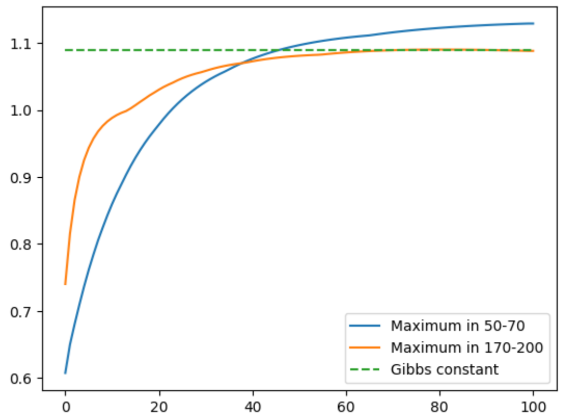

Figure 8: The relative overshoot at fist up jump and last down jump (at x coordinates 50 and 205) at row 170 on the cylindrical phantom.

It is clear that the first overshoot systematically exceeds the classical 1d overshoot value, indicated by the dashed line, because the phantom is vertically inhomogeneous. In contrast, the second discontinuity (analysed in the interval 170-200) exhibits behaviour that matches theoretical expectations, since the phantom is locally vertically homogeneous at these points.

Video 9 presented below gives another visualisation of the Gibbs effect. The sequence of the reconstruction images are displayed, showing the progression of the iteration. As the iteration goes, a brightening becomes visible along the boundary of the phantom, corresponding to the overshoot. Based on the preceding analysis the brightening is more pronounced in regions where the cylinder wall is thinner. Although this effect could be subtle to the naked eye.

(For QR code, see "List of Videos" on page vi.)

Figure 9: The reconstruction series of the cylindrical phantom.

4.1.2 Convergence of Fourier components

This section is about the analysis of the Fourier components of the original image and the images produces by the MLEM iteration. Among the Fourier components, the four Fourier matrices (α, β, γ and δ) are responsible for the two-dimensional effects, therefore these are selected for detailed examination.

The figure 10 below illustrates the relative deviation of the Fourier matrices. In the nth iteration the quantity $\dfrac{\|\alpha_n - \alpha_0\|_{\mathrm{HS}}}{\|\alpha_0\|_{\mathrm{HS}}}$ is plotted, where $\|\cdot\|_{\mathrm{HS}}$ denotes the Hilbert-Schmidt norm of a matrix, that is $\|A\|_{\mathrm{HS}} = \operatorname{Tr} A^* A = \displaystyle\sum_{i,j=1}^{N} |A_{ij}|^2$.

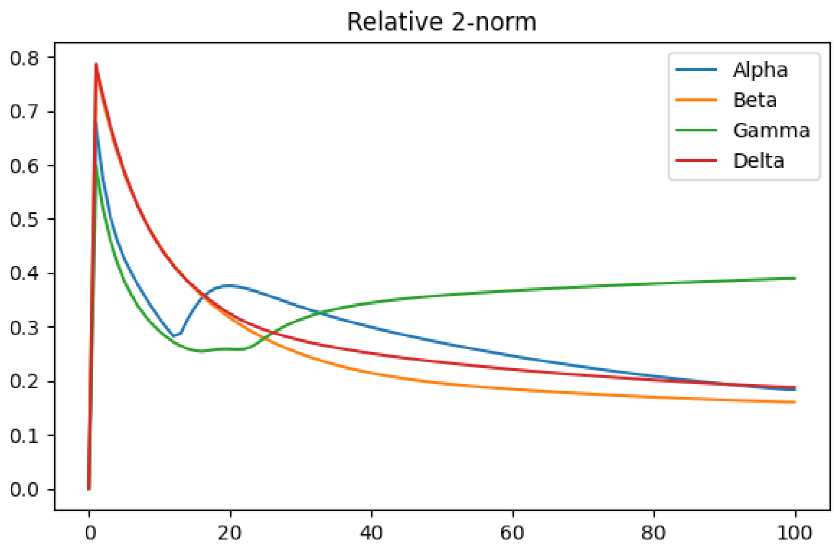

Figure 10: The relative errors of the Fourier coefficient matrices as a function of iteration number.

It can be observed that each Fourier matrix undergoes a transient phase at the beginning of the iteration. The β and δ coefficients evolve as expected, according to a monotone decreasing sequence. Providing a straightforward theoretical explanation for the local maximum observed in the behaviour of the α component around the 20th iteration is not trivial, nor is it for the monotonic increase of the γ component. It is plausible that the γ component also reaches a local maximum at a later stage, followed by a decrease.

Next, those elements of the Fourier matrices the nth image are illustrated, which are close to the corresponding components of the Fourier matrix of the original image. The method is presented in detail for matrix α, naturally the same procedure was applied to the other three matrices too. The comparison was performed using two parameters. The parameter minval was used to select those elements of the Fourier matrix of the original image whose absolute values exceed the threshold defined by minval.

$$\alpha^{(0)}_{\text{minval}} = \left\{(i,j) \in \{1,\dots,N\}^2 \mid \left|\alpha^{(0)}_{ij}\right| \geq \text{minval}\right\} \tag{7}$$

Second, the parameter err $\in [0,1]$, was used to identify those elements of $\alpha^{(n)}$, which are in a relative neighbourhood with err radius of the corresponding components of the original image.

$$\alpha^{(n)}_{\text{minval,err}} = \left\{(i,j) \in \{1,\dots,N\}^2 \mid \left|\alpha^{(0)}_{ij}\right| \geq \text{minval}, \left|\alpha^{(n)}_{ij} - \alpha^{(0)}_{ij}\right| < \left|\alpha^{(0)}_{ij}\right| \text{err}\right\} \tag{8}$$

An α_{ij} Fourier component will be called good (with respect to minval and err) if $ij \in \alpha^{(n)}_{\text{minval,err}}$.

On the Figure 11 grey means that the absolute value of the Fourier components of the original image is greater than 0.1; and, black marks those Fourier components of the 100th image that are within a 25% relative neighbourhood of the original one.

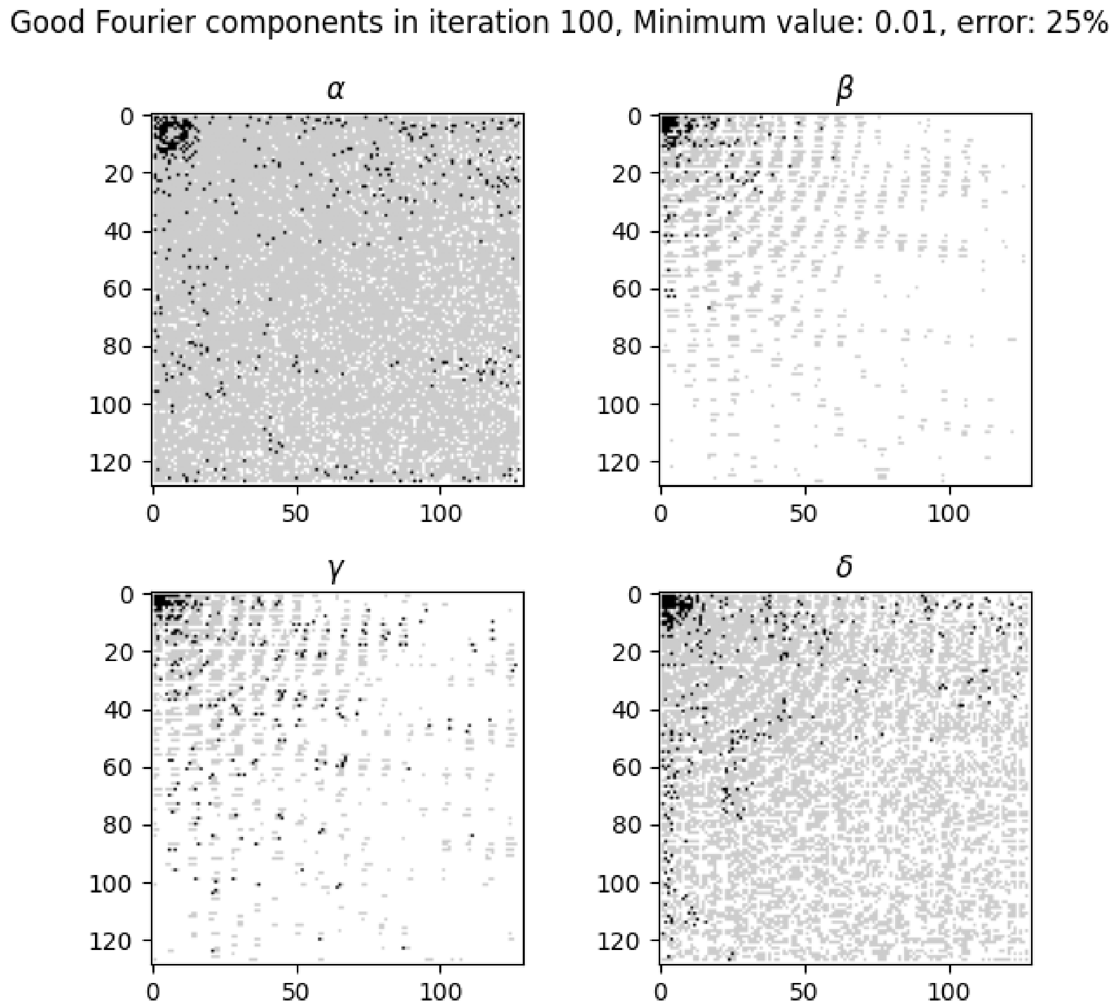

Figure 11: The four Fourier coefficient matrix of the 100th iteration: shaded grey, where the Fourier components of the original image is greater than 0.1; and black, where marks those Fourier components of the 100th image that are within a 25% relative neighbourhood of the original one.

It is worth to examine how the locations of the reconstructed Fourier components evolve during the iteration. One might naturally assume that the number of accurate Fourier components increases over time simply by accumulating new components next the good ones. This trend can be observed in the video below, but it is also evident that the convergence behaviour is considerably more intricate.

Video 12 suggests that the low-frequency components are reconstructed first, and after progressively the higher-frequencies. It is important to emphasise, that this is not a strict rule, but rather an observable trend in the convergence process, next to other patterns which are more difficult to characterise.

(For QR code, see "List of Videos" on page vi.)

Figure 12: The good Fourier components of the Fourier matrices through iterations.

A method was mentioned above for comparing the coefficients of the Fourier matrix at the n-th iteration with the original one. This comparison method may appear natural, it is worths to examine how the ratio of the good Fourier components varies under this criterion for different minimum values. The ratio

$$\frac{\left|\alpha^{(n)}_{\text{minval,err}}\right|}{\left|\alpha^{(0)}_{\text{minval}}\right|} \tag{9}$$

is plotted in Figure 13.

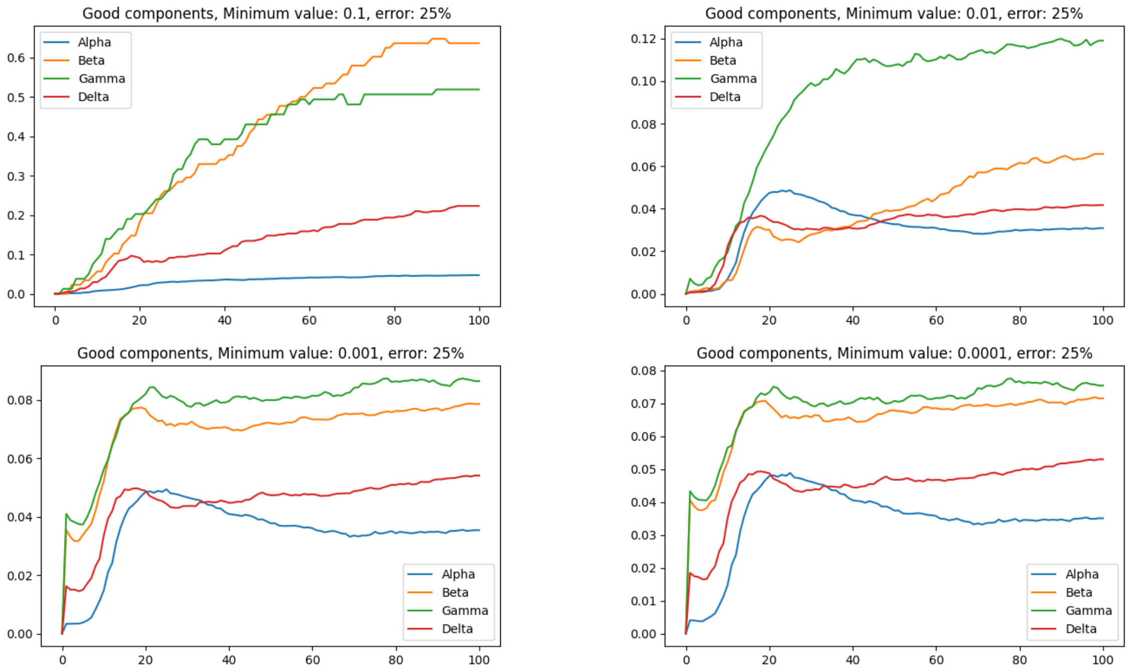

Figure 13: The ratio of the good Fourier matrix coefficients as a function of the iteration number. The relative error for the Fourier matrices is 25%, while the value of the Fourier components changes from 10^{-4} to 10^{-1} minimum absolute value.

The err $= 0.1$ case is shown in Figure 14.

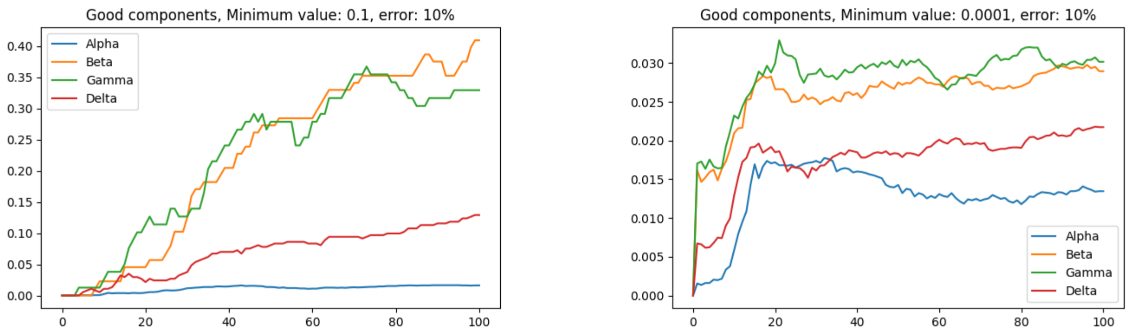

Figure 14: The ratio of the good Fourier matrix coefficients as a function of the iteration number. The error is 10% and the minimum absolute value of the Fourier components are 10^{-4} and 10^{-1}.

It is evident from the figures that the ratio of good Fourier components, as a function of the number of iterations, depends strongly on the chosen parameters minval and err. This dependence is not limited to the absolute values, which is expected (for example, a stricter error criterion naturally results fewer good components), but is also reflected in the overall trends of the curves.

There is another approach to the analysis of Fourier matrices: The ij-th harmonic components are characterised by the quantities α_{ij}, β_{ij}, γ_{ij} and δ_{ij}, or short by the vector $v_{ij} = (\alpha_{ij}, \beta_{ij}, \gamma_{ij}, \delta_{ij})$, which will be called to amplitude vector of the ij-th harmonic. From the Fourier matrices of the image obtained in the n-th iteration, one can construct the matrix $V^{(n)}$, whose ij-th element is the four-dimensional vector $v_{ij}^{(n)}$ defined above. (The case $n = 0$ corresponds to the original image, i.e., the phantom.) As done before, first select those elements of the matrix $V^{(0)}$, whose norm ($\|x\| = \sqrt{\sum_{k=1}^{n} x_k^2}$) exceed a threshold denoted by minnorm.

$$V_{\text{minnorm}}^{(0)} = \left\{(i,j) \in \{1,\dots,N\}^2 \mid \left\|v_{ij}^{(0)}\right\| \geq \text{minnorm}\right\}$$

Second, identify those elements of $V^{(n)}$, which are in a relative neighbourhood with err radius of the corresponding components of the original image.

$$V_{\text{minnorm,err}}^{(n)} = \left\{(i,j) \in \{1,\dots,N\}^2 \mid \left\|v_{ij}^{(0)}\right\| \geq \text{minnorm},\ \left\|v_{ij}^{(n)} - v_{ij}^{(0)}\right\| < \left\|v_{ij}^{(0)}\right\| \text{err}\right\}$$

A v_{ij} harmonic vector called to be a good harmonic vector, if $(i,j) \in V_{\text{minnorm,err}}^{(n)}$.

The ratio

$$\frac{\left|V_{\text{minnorm,err}}^{(n)}\right|}{\left|V_{\text{minnorm}}^{(0)}\right|}$$

is shown in Figure 15 as a function of the iteration number n.

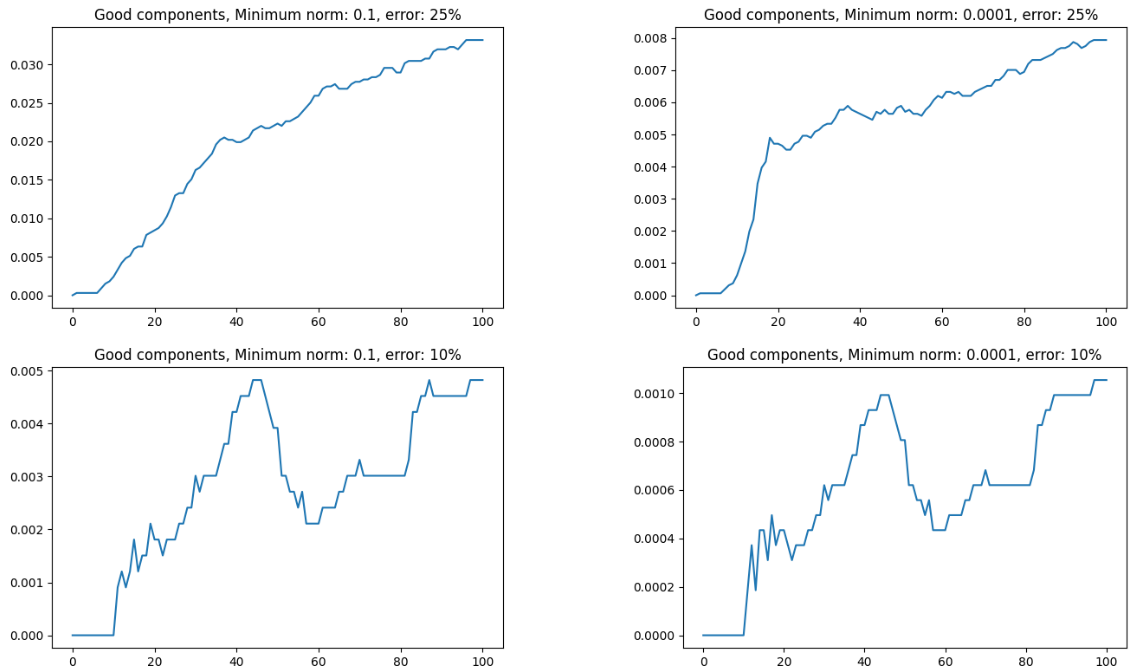

Figure 15: The ratio of the good harmonic vectors as a function of the iteration number. The relative error for the Fourier matrices is 25% and 10%, while the minimum norm of harmonic vectors is 10^{-1} and 10^{-4}.

When the number of the good harmonic vectors as a function of the iteration was examined using a 25% relative error threshold, the resulting graph corresponded well to the naive prior expectation. Specifically, after a minor smoothing effect, the number of well enough reconstructed harmonic vectors increased monotonically with the number of iterations. In contrast, the behaviour observed for the 10% relative error threshold was markedly different. In this case, the number of good harmonic vectors had a local maximum around iterations 45-46, followed by a steep decline. These graphs suggest that, only with particular care one can state that the MLEM algorithm operates by progressively restoring an increasing number of the Fourier components.

Returning to the 25% error threshold, which yielded the more well-behaved results, Video 16 illustrates which Fourier vectors are successfully reconstructed as a function of the iteration number. From this, it can also be inferred that the reconstruction process exhibits a general tendency to recover progressively higher-frequency components. Naturally, this should be regarded only as a broad trend rather than a strict rule.

(For QR code, see "List of Videos" on page vi.)

Figure 16: The good Fourier vectors (with threshold minnorm = 0.1 and err = 0.25) through iterations for the sectoral phantom.

One of the main conclusions of this subsection is that the dependence of the number of well reconstructed Fourier components on the iteration number is remarkably complex. This observation may have several possible interpretations. It may indicate that the analysis of Fourier components is not an adequate tool for studying convergence; or, it may suggest that the definition of good Fourier components should be redefined; or a different grouping of the Fourier coefficients would lead to a more meaningful results.

4.2 Sectoral phantom

In this section, the reconstruction properties of the "sectoral" phantom (family) are presented. The phantom itself is a circular sector whose centre coincides with the centre of the region of interest (ROI), and it can be characterised by four parameters: a relative radius (equal to 1 if it reaches the boundary of the ROI);
the central angle of the sector (ranging from 0 to 360 degrees);
and two activity values: the background and the sector.

In the following, the relative radius is fixed at 0.7 (which corresponds to a radius of 90 pixels for a resolution of 256×256), and the background activity is fixed at 20.

4.2.1 A representative case study from the sectoral phantom family

In this subsection the phantom with central angle 125° and activity levels 20 and 70 is studied. Figure 17 shows the phantom and it's reconstructed image after 100 iteration.

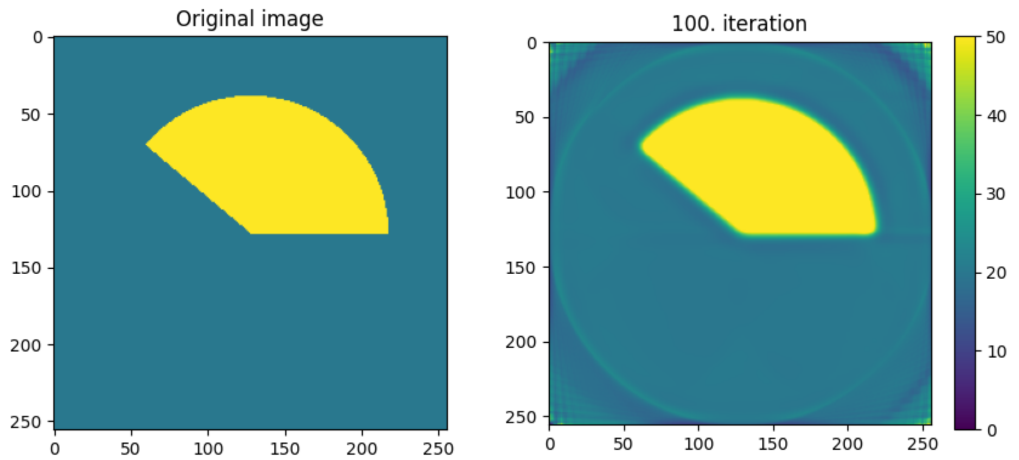

Figure 17: A sectoral phantom with central angle 125° and activity values 20 and 70, and it's reconstruction.

The figure 18 shows that, in the case of this phantom, following an initial transient phase, the relative error of the Fourier coefficient matrices decreases monotonically with the number of iterations. However, it is also worth noting the previously observed interesting behaviour of the parameter γ: around the 12th iteration, the relative error has a local minimum, after which the relative error begins to increase again, and later subsequently decreases to a level below that earlier local minimum.

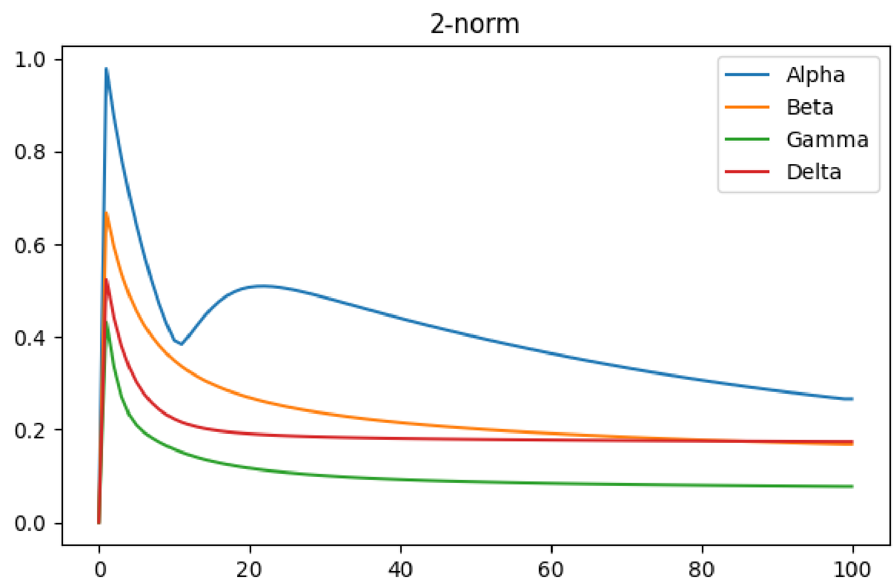

Figure 18: The relative errors of the Fourier coefficient matrices as a function of the iteration number.

Video 19 confirms the phenomenon observed for the cylindrical phantom: when examining the correctly reconstructed components of the Fourier matrix as a function of the iteration number, the low-frequency components are recovered first, followed by higher-frequency components. As can be seen, this is just a rough idea, the reconstruction of the Fourier components follows a more complex, still unknown, pattern.

(For QR code, see "List of Videos" on page vi.)

Figure 19: The good Fourier components of the Fourier matrices through iterations for the sectoral phantom.

The Figure 20 once again demonstrates how different the behaviour of the number of correctly reconstructed Fourier components can be as a function of the iteration count. It can be observed, for instance, that in the case of parameter δ, the character of the curve changes significantly depending on whether the threshold is set to 10^{-1} or to 10^{-2}. Similarly, for parameter β, the number of correctly reconstructed components increases monotonically with the number of iterations when the error threshold is 10^{-1} or 10^{-2}; however, for smaller thresholds (10^{-3}, 10^{-4}) a local maximum appears in the number of good components at 20 iterations, which is not achieved again in the next 80 iterations.

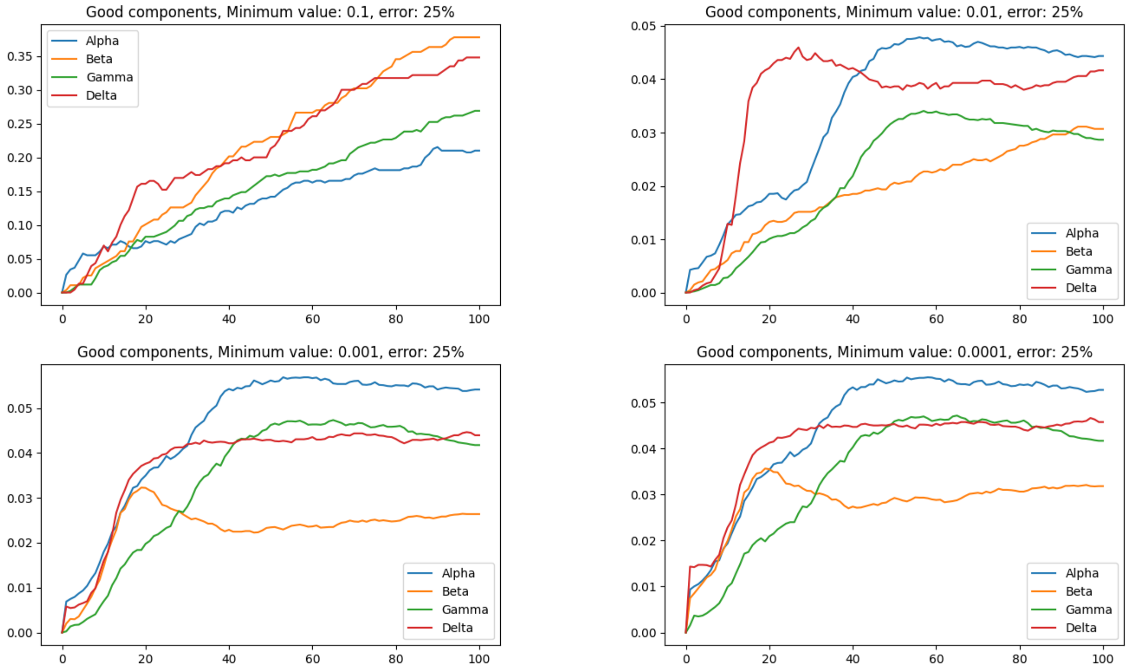

Figure 20: The ratio of the good Fourier matrix coefficients as a function of the iteration number for the sectoral phantom. The relative error for the Fourier matrices is 25%, while the value of the Fourier components changes from 10^{-4} to 10^{-1} minimum absolute value.

Figure 21 shows different circular sections of the phantom and the reconstructed image after 100 iteration. The circular sections were made according to circles with centre at pixel $(128, 128)$ and with different radiuses in clockwise direction and that circle was discretized to 128 pixels. The radius of the phantom is 90 pixels. As shown in the figure, the reconstructed image produces the Gibbs phenomenon when the radius is between 15 and 85. Moreover, it can be observed that the reconstructed activity begins to decrease before the radius reaching 90 pixels, and only approaches the background level at 94 pixels.

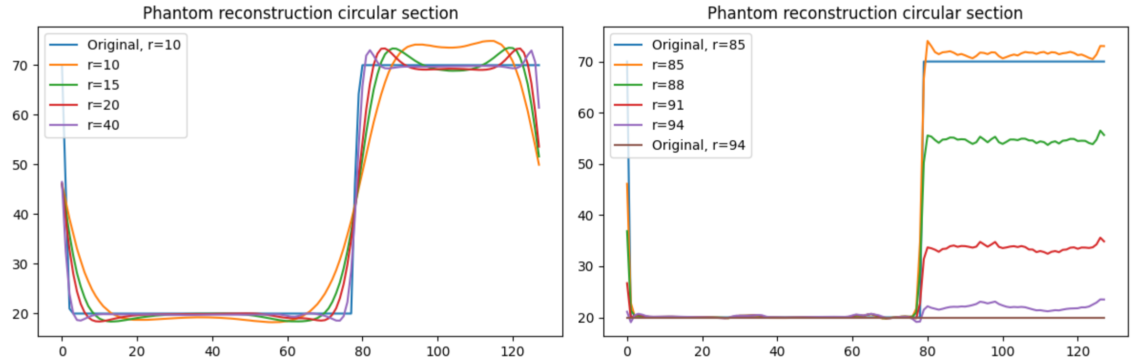

Figure 21: Circular sections of the sectoral phantom.

4.2.2 Family of sectoral phantoms

The reconstruction of the phantom was investigated for different intensity parameters and central angles. The central angle was varied from 5° to 355° in steps of 5°, and the background intensity was fixed at 20, while the phantom intensity was varied from 30 to 100 in steps 10. That is, the first parameter can take values in the set $\{0, 1, \ldots, 70\}$, corresponding linearly to the scale of the central angle, and similarly the second parameter has values in $\{0, 1, \ldots, 7\}$. The resulting parameter space is illustrated in Figure 22.

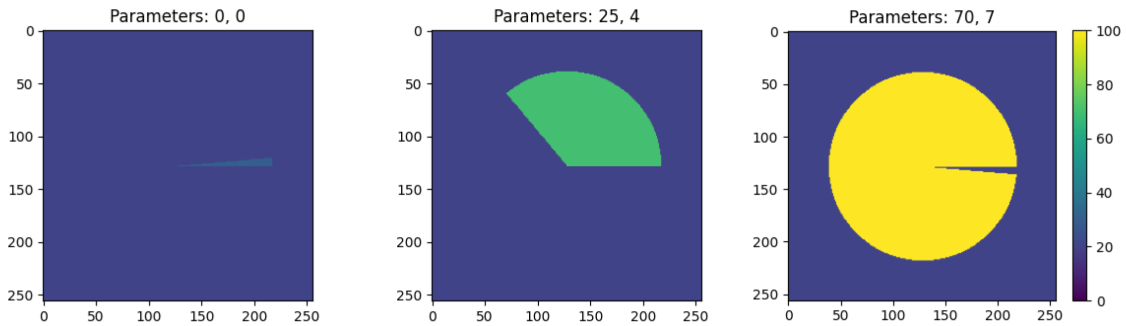

Figure 22: Parameter space of the sectoral phantom set.

Figure 23 shows the relative number of restored Fourier matrix components after 100 iteration as a function of the phantom parameters. In this setting, those Fourier matrix components were examined whose absolute value was at least minval $= 0.05$, and a component was considered correct if it fell within a err $= 0.2$ tolerance of the original value. It can be observed for all matrices, that the lower the phantom activity corresponds to more restored Fourier matrix components (among greater than 0.05 absolute value components and for 20% tolerance level) over 100 iterations.

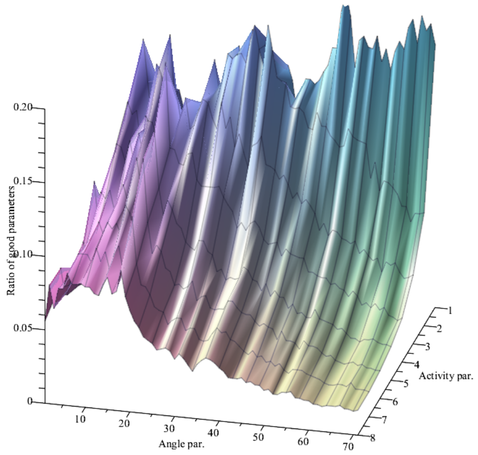

Matrix α.

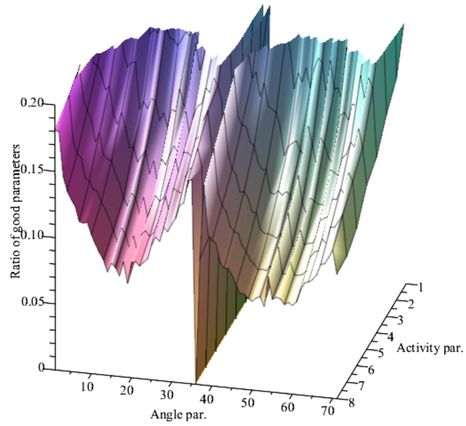

Matrix β.

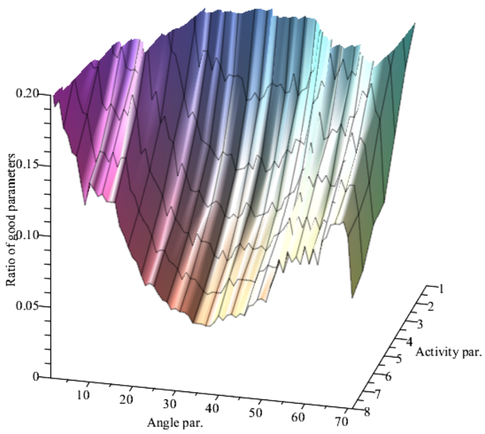

Matrix γ.

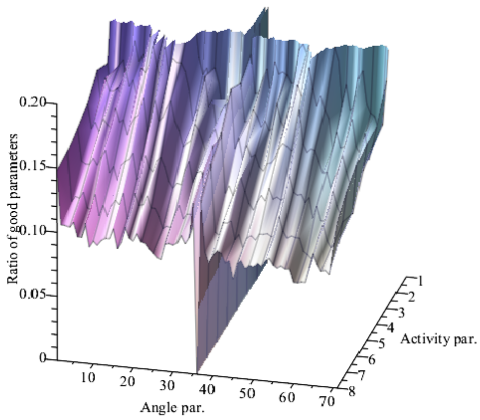

Matrix δ.

Figure 23: The ratio of good Fourier matrix components after 100 iteration as a function of the phantom parameters. Matrix components with absolute values greater than 0.05 were taken into account and the tolerance level was 15 %.

Figure 24 show the relative 2-norm errors of Fourier matrices after 100 iterations. For the relative error of the Fourier components, the opposite effect can be observed to that seen for the number of good Fourier components. The relative error decreases as the phantom activity increases. This phenomenon is independent of the central angle of the phantom.

As shown in the figure, at certain angular parameters the relative errors have special behaviour. A possible explanation is that, due to the way the central angle of the phantom was varied, the phantom had special symmetry, which caused special Fourier matrices; for example in some cases, certain Fourier matrices may even be zero. Consequently, these cases cannot be considered representative behaviour.

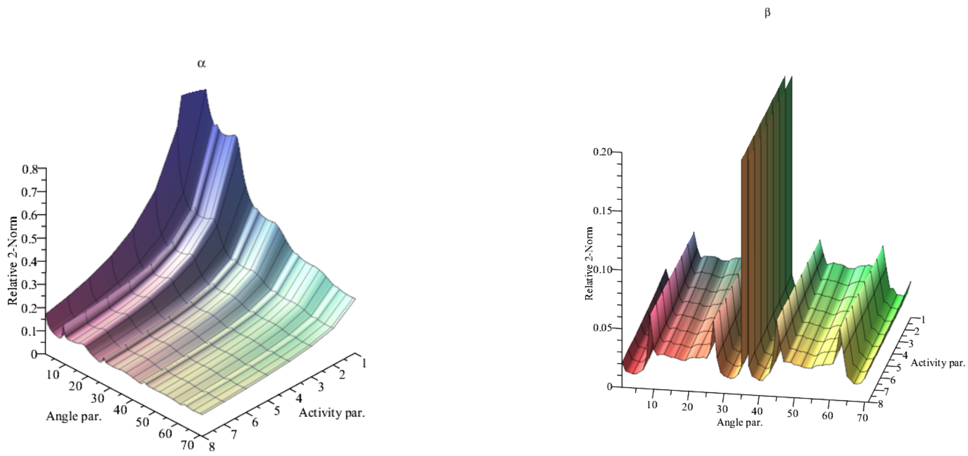

Matrix α.

Matrix β.

Figure 24: The relative 2-norm errors of the Fourier matrices after 100 iteration as a function of the phantom parameters.

5 Plans for future research

5.1 Phantom families

In the previous section, the reconstruction of the cylindrical phantom set and the sectoral phantom set was analysed. In the course of this thesis work, however, the reconstruction of two additional phantom families was also carried out. Furthermore, for each phantom family, measurement datasets were also generated in the presence of Poisson noise, and their corresponding reconstructions (precisely the first 100 iterative reconstruction steps) have been done. A brief overview of two additional phantom families is presented below.

5.1.1 Circular phantom set

In this phantom family, the phantom consists of a circle located at the centre of the ROI, partitioned into two alternating types of circular sectors. In principle, the phantom is characterised by five parameters:
– three activity parameters: the background activity and the activity values of the two types of circular sectors; – the radius of the circle; – the number of circular sectors.

Among these parameters, two activity values were fixed (the background activity at 0.4 and the more active sector value at 1.2), as well as the radius, which was set to 85% of half the ROI size. The number of circular sectors varied in $\{6, 8, \ldots, 40\}$, while the activity value of the moderately active sectors was allowed to take values in $\{0.5, 0.6, \ldots, 1.1\}$.

The resulting parameter space is illustrated in Figure 25.

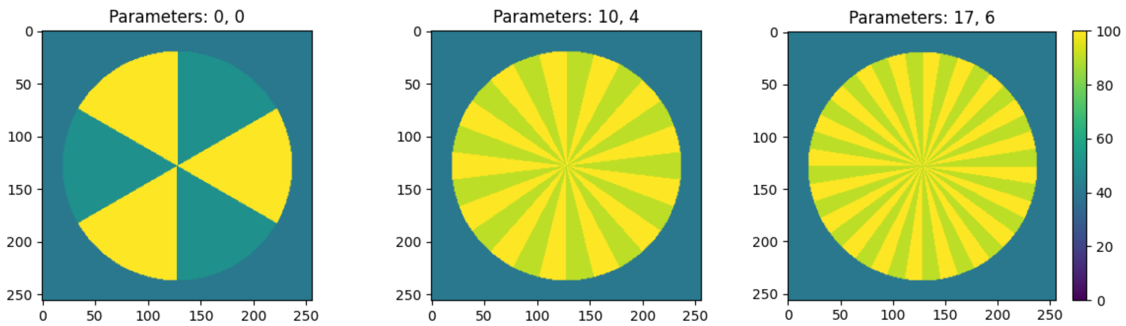

Figure 25: Parameter space of the sectoral phantom set.

One example for reconstruction can be seen in Figure 26, where the number of sectors is 26, and the activity values are 0.4, 0.8 and 1.2.

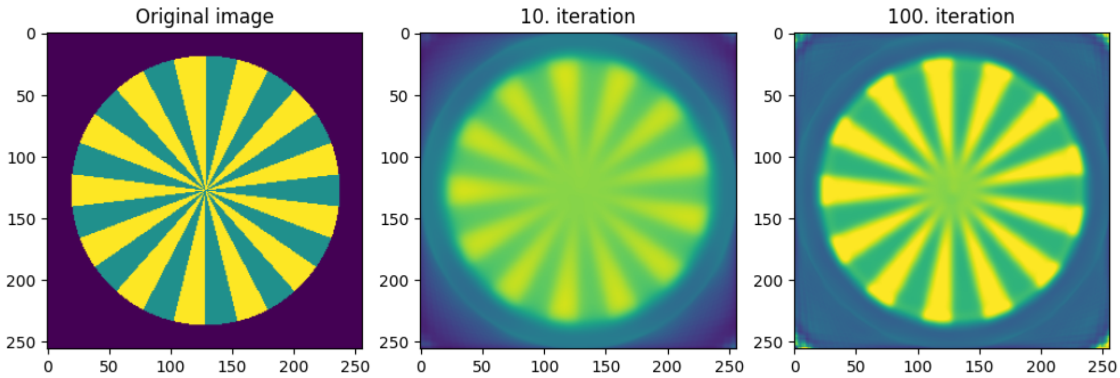

Figure 26: An example for the sectoral phantom and its reconstruction.

A wide range of questions may be investigated in connection with this phantom family. For example, one can study at which iteration number and radius, the circular sectors begin to become clearly distinguishable, as well as how the Gibbs phenomenon depends on the properties of the sectors, the radius, and the number of iterations.

It would be important to define objective quantitative measures for all of these properties. For instance, a precise criterion would be required to determine what is meant by the sectors being "distinguishable". The difficulty of this issue is illustrated in Video 27 below, in which, based on the 100th iteration of the phantom described above, the reconstructed activity values are displayed along tangential directions at different radii moving outward from the centre of the phantom, together with the reference activity distribution of the phantom itself.

(For QR code, see "List of Videos" on page vi.)

Figure 27: Activity values of the 100th iteration of the above mentioned phantom at different radii.

It can be observed that, for radii smaller than 15, only a few sectors are visible even after 100 iterations. However, when the radius exceeds 24, all sectors become detectable, although only with very small differences in activity values, meaning that they would likely not be distinguishable by visual inspection alone.

5.1.2 Chessboard phantom set

At this phantom family, only two activity parameter is used and the phantom geometry follows a checkerboard-like pattern; however, in this case, the sizes of the individual cells vary according to an arithmetic progression. In this case, a total of 36 phantom reconstructions are available, from which it is hoped that information can be extracted regarding how regions of differing activity, alternating at various spatial distances, are reconstructed. Without going into unnecessary mathematical details on phantom cells sizes, some representative examples from this phantom family are shown in Figure 28.

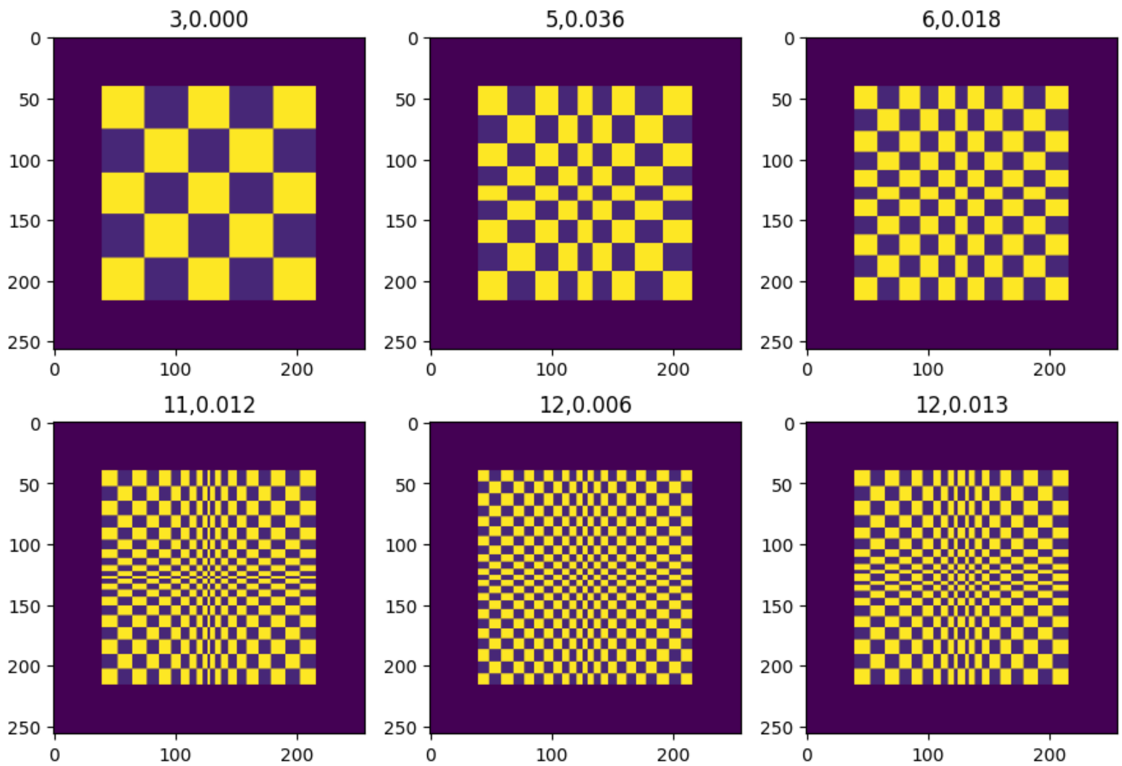

Figure 28: Some representative phantom from the chessboard phantom set.

5.2 Theoretical considerations

The two-dimensional Gibbs phenomenon was previously studied through the analysis of Fourier components. However, it may be promising to determine the eigenfunctions of the Forward Projection and Backward Projection transformations (most likely only numerically obtainable), and to study the emergence of the Gibbs phenomenon, and the reconstruction behaviour of the components in this function basis.

Furthermore, numerous additional theoretical approaches may be considered for studying the formation of the Gibbs phenomenon, such as the local evaluation of various entropies and relative entropies, the computation of local Fisher information and informationgeometrical quantities, and the analysis of the effects of small perturbations. The characterisation of these quantities may contribute to a deeper understanding of the nature of the Gibbs phenomenon in the absence of (Poisson) noise; however, the primary challenge lies in understanding how noise influences the the Gibbs phenomenon.

Conclusion

> Everything should be made as simple as possible, but not simpler.
>
> Albert Einstein

One of the main conclusions regarding the convergence of Fourier coefficients in iterative SPECT reconstruction is that the Fourier coefficients has highly complex behaviour as a function of the iteration number.

Based on the investigations carried out so far, the following observations can be made.

1. It can be observed that during the iterative process, the coefficients corresponding to lower harmonics tend to be reconstructed earlier than those associated with higher harmonics. This should not be interpreted as a strict ordering, but rather as a general tendency.

2. Consider a quantity that measures how many harmonic coefficients have been reconstructed within a prescribed relative error after a given number of iterations. In most cases, this quantity increases monotonically with the iteration number. However, in some cases, after reaching a local maximum, it decreases temporarily before resuming a monotonic increase.

3. This latter phenomenon questions the applicability of this otherwise intuitive quantity. As a possible direction for further investigation, one may consider defining neighbourhoods of the coefficients with respect to some nontrivial metric, or, studying the convergence of coefficients in a different eigenfunction system instead of the Fourier basis.

4. During the image reconstruction process, it was observed that, in several cases, the MLEM algorithm reproduced the exact magnitude of the Gibbs overshoot after a sufficiently large number of iterations. However, without exception, this phenomenon was observed only for positive overshoots. In the reconstruction of the background activity, a decrease of comparable magnitude preceding a sharp transition was never observed relative to the positive overshoot appearing after the transition. This suggests that the distance between activity values should perhaps not be interpreted in terms of the conventional absolute difference, but rather through some alternative metric arising naturally from the underlying model.

Bibliography

[1] Maxime Bôcher. Introduction to the Theory of Fourier's Series. *Annals of Mathematics*, 7(2/3):81–152, 1906.

[2] A. P. Dempster, N. M. Laird, and D. B. Rubin. Maximum Likelihood from Incomplete Data via the EM Algorithm. *Journal of the Royal Statistical Society. Series B (Methodological)*, 39(1):1–38, 1977.

[3] engineerguy. An Old Mechanical Computer: The Harmonic Analyzer. YouTube video, 2016. Accessed: 2026-04-30.

[4] J. Willard Gibbs. Fourier's Series. *Nature*, 59(1539):606–606, 1899.

[5] B. Hammack, S. Kranz, and B. Carpenter. *Albert Michelson's Harmonic Analyzer: A Visual Tour of a Nineteenth Century Machine That Performs Fourier Analysis*. Articulate Noise Books, 2014.

[6] O. Israel, O. Pellet, L. Biassoni, D. De Palma, E. Estrada-Lobato, G. Gnanasegaran, T. Kuwert, C. la Fougere, G. Mariani, S. Massalha, D. Paez, and F. Giammarile. Two decades of SPECT/CT - the coming of age of a technology: An updated review of literature evidence. *European Journal of Nuclear Medicine and Molecular Imaging*, 46(10):1990–2012, 2019.

[7] Cornelius Lanczos. *Discourse on Fourier Series*. Hafner Publishing Company, New York, 1966. Also published by Oliver & Boyd, Edinburgh.

[8] L. A. Shepp and Y. Vardi. Maximum Likelihood Reconstruction for Emission Tomography. *IEEE Transactions on Medical Imaging*, 1(2):113–122, 1982.

[9] Henry Wilbraham. On a certain periodic function. *The Cambridge and Dublin Mathematical Journal*, 3:198–201, 1848.

[10] Ádám Zlehovszky. *Total Variation regularized SPECT reconstruction with Primal-Dual Hybrid Gradient method*. PhD thesis, ELTE, Scientific Computing and Models, Numerical and Symbolic Methods, 2025.